A Comprehensive Set of Impact Data for Common Aerospace Metals

M. R. W. Brake*
William Marsh Rice University
Houston, TX 77005

P. L. Reu, and D. S. Aragon
Sandia National Laboratories†
Albuquerque, NM 87185

ABSTRACT

The results of two sets of impact experiments are reported within. To assist with model development using the impact data reported, the materials are mechanically characterized using a series of standard experiments. The first set of impact data comes from a series of coefficient of restitution experiments, in which a 2 meter long pendulum is used to study "in context" measurements of the coefficient of restitution for eight different materials (6061-T6 Aluminum, Phosphor Bronze alloy 510, Hiperco, Nitronic 60A, Stainless Steel 304, Titanium, Copper, and Annealed Copper). The coefficient of restitution is measured via two different techniques: digital image correlation and laser Doppler vibrometry. Due to the strong agreement of the two different methods, only results from the digital image correlation are reported. The coefficient of restitution experiments are "in context" as the scales of the geometry and impact velocities are representative of common features in the motivating application for this research. Finally, a series of compliance measurements are detailed for the same set of materials. The compliance measurements are conducted using both nano-indentation and micro-indentation machines, providing sub-nm displacement resolution and μN force resolution. Good agreement is seen for load levels spanned by both machines. As the transition from elastic to plastic behavior occurs at contact displacements on the order of 30 nm, this data set provides a unique insight into the transitionary region.

1 Introduction

Impact is a process common to many mechanical systems, both externally in terms of applied loads and internally in terms of interacting components. Impacts, whether by design or unintentional consequence, have profound effects on a system's dynamics including potential nonlinear responses [1], energy dissipation [2], wear [3], and failure [4]. Many electro-mechanical components contain parts such as gears and pawls that contact one another through normal operation (and sometimes unintentionally too). This contact serves to dissipate energy in the system via multiple processes such as plastic flow, dislocation of grain boundaries, fracture of asperities, generation of new surfaces, etc. To model each of these processes in high fidelity would create a prohibitively large simulation that would prevent design through analysis. One solution to this problem is to replace the high fidelity, spatially distributed physics of contact with a single degree of freedom (SDOF) constitutive model [5–9] that captures the effects of contact at the meso and macro scales[1]. The choice in contact model, however, can have a profound effect on the design and performance of a system [14].

By necessity, SDOF constitutive models neglect many of the nano-scale (and some of the micro-scale) mechanisms that dissipate energy during contact or an impact event. Thus, these models must be validated against in-context experiments to ensure that they accurately predict the phenomenon of interest. The SDOF constitutive model calculates the interfacial

*Corresponding author; brake@rice.edu

†Sandia National Laboratories is a multi-mission laboratory managed and operated by Sandia Corporation, a wholly owned subsidiary of Lockheed Martin Company, for the U. S. Department of Energy's National Nuclear Security Administration under Contract DE-AC04-94AL85000.

[1]For inelastic models, see [10–13] as examples.

force, pressure, and contact area as functions of the interference (contact displacement). These models may be directly validated using compliance measurements of the force-displacement curves for a material, but it is not immediately obvious how discrepancies between the model and measured compliance curves affect the models ability to predict dissipation. For instance, an SDOF model could nearly match the loading portion of the compliance curve and have a small discrepancy in the restitutive regime, but have higher error in predicting the coefficient of restitution (COR). Conversely, a model could show very poor agreement for all aspects of the compliance curves but due to the integration over the entire impact event, it could accurately predict dissipation curves. Therefore both direct (in terms of quantities principally calculated by the model such as the compliance curves) and indirect (such as derived quantities like the COR) validation metrics are needed.

A limitation of the existing studies of energy dissipation is a lack of experimental validation. The existing literature on measurements of energy dissipation in elastic-plastic materials is limited and can be divided into two categories: COR experiments and compliance measurements. The first type of COR experiment is an anvil-based experiments, consisting of measuring the displacement of a ball dropped vertically against a nominally flat, horizontal anvil. In particular, [15, 16] studied 5 mm diameter spheres of aluminium oxide dropped from various heights against anvils made out of aluminum alloy or EN9 steel. A second type of COR experiment is pendulum-based experiments, featuring two spheres suspended as pendulums that impact each other; typically, one sphere is at rest and the second sphere is given an initial displacement. Existing studies have used SUJ2 steel [17], and brass, lead, glass, porcelain, and agate [18]. More recently, high velocity impact experiments were conducted using an air gun [19] that shoots one sphere towards a second. The instrumentation for COR studies have mostly been digital cameras [15,17,18] operating at 30 frames per second or less. More recent experiments have used laser interferometry and photo transistors [19], though even these methods are limited in resolution.

Compliance measurements, on the other hand, do not directly measure the energy dissipated, but rather infer it from the hysteretic measurement of contact force in the loading and unloading of a test specimen [20–26]. These experiments are conceptually divided into two categories as well: the compression of a compliant sphere by a rigid surface (at least, rigid compared to the compliant sphere) [23], and the indentation of a compliant surface by a rigid sphere [26]. Theoretical models in the literature have argued that these two separate cases must be modeled differently [27]; however, other models have successfully been able to predict both cases with the same model (e.g. [5, 6]).

Impact events are localized, which means that they may be influenced by local properties such as the distribution of asperities, grain boundaries and dislocations, and material structure near the contact zone. Fortunately, previous efforts to validate constitutive models have shown that the majority of the response can be captured using bulk properties of the material [6] (e.g. properties measured at the macroscale, such as the elastic modulus). The influence of local properties, thus, are hypothesized to be relegated to explaining the variance observed in experimental data. One gap that is present in most experiments is that an incomplete set of bulk properties is reported for the material specimen. As new contact models require information that is not thought of as germane in older experiments (such as material hardness), validation becomes a difficult task.

This paper seeks to bridge this gap by providing multiple sets of information for the specimen tested: material characterizations (§2), COR data (§3), and compliance measurements (§4).

2 Test Specimen and Characterization

In the following experiments, eight different materials are characterized: 6061-T6 Aluminum (Al), Phosphor Bronze alloy 510 (PhB), Nitronic 60A (N60), Stainless Steel 304 (SS304), Titanium (Ti), Copper (Cu), Annealed Copper (AnCu), and Hiperco (Hi). The Hiperco was conditioned according to the heat treatment schedule AYA5597[2]. These materials were chosen to span a range of different materials used in aerospace applications. All material specimen (for both characterization and experiments) were fabricated from the same source of stock, ensuring that the variability associated with different lots of material was negated.

2.1 Tensile Testing

Tests were completed on 24 cylindrical tensile samples with specimens comprising three samples from each of the eight materials (note, however, that results from two of the materials – Cu and Ti – were not available at the time of publication). All tests were performed using a MTS 22 kip (98 kN) load frame. Data acquisition for actuator stroke, load, auxiliary load, an external grip LVDT, an extensometer, and time was taken at a frequency of 10 Hz. A typical test setup is shown in Fig. 1.

Modifications to the test setup shown in Fig. 1 were required to accommodate a full tensile pull to failure of the AnCu specimens. Due to the material's low yield strength and geometry of the tensile specimen, the first AnCu sample tested did not complete the test procedure. Instead, failure was observed within the threaded area from plastic deformation of the

[2]The specimen are cleaned and placed in an oven; a vacuum is pulled to 1 μm of mercury absolute or less for 15 minutes without heating, and held throughout the subsequent heating cycles; the oven is heated to 316°C, ±25°C, and held for 15-30 minutes; next, the oven is heated to 500°C, ±25°C, and held for 30 minutes; then the oven is heated to 864°C, ±25°C, and held for 2-4 hours; finally, the specimen are cooled at a rate of 140°C, ±50°C, per hour until 300°C, and any rate thereafter.

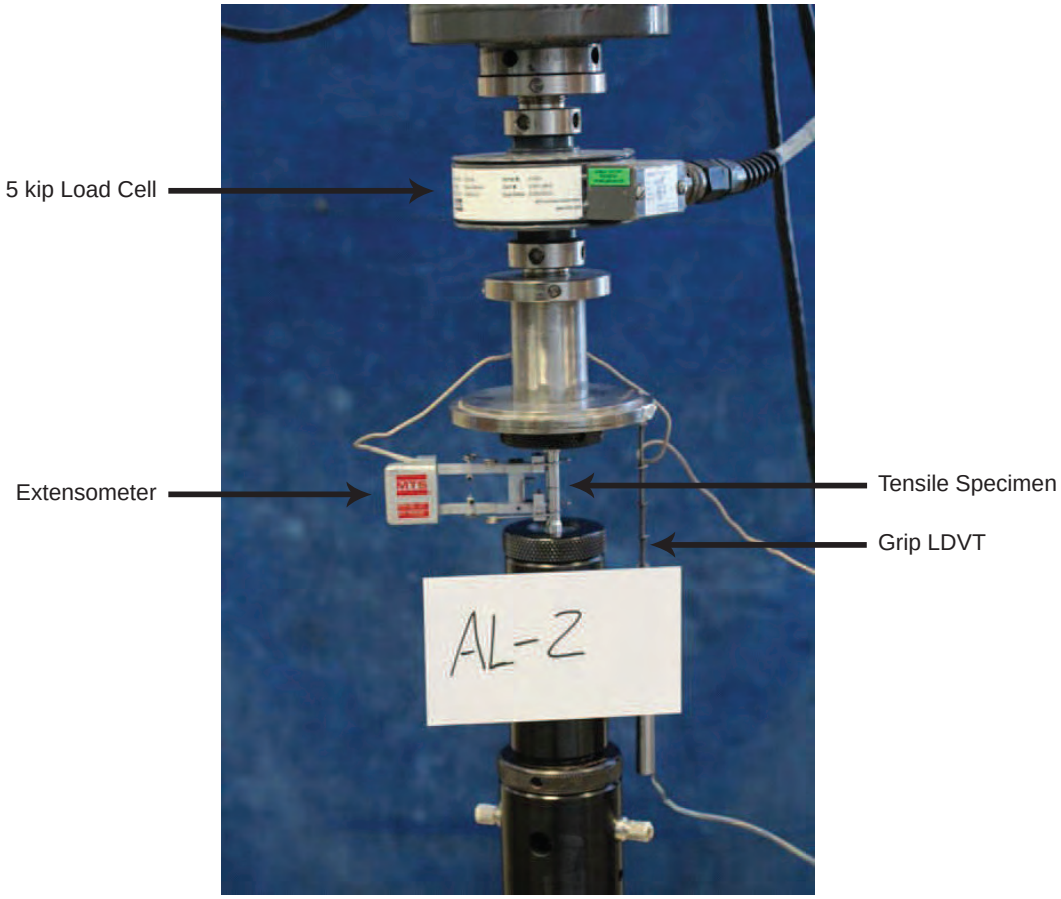

Fig. 1. Typical tensile test setup.

threads resulting in separation of the AnCu sample from the test fixture. To address this, a nut was threaded on and soldered to each end of the AnCu specimens and a bolt test fixture with washers was utilized for the test, allowing the added nuts to interface with the washers. This modified test setup was successful, supplementing material properties obtained from the first run.

Following ASTM E8 standards, a stress rate of 10-100 ksi/min (69-690 MPa/min) was specified, thus a Grip LVDT pull rate of 0.2 mil/sec (0.0051 mm/sec) was commanded for all tests, allowing each material to fall within the specified range of stress rate. The commanded stress rate resulted in targeted average stress rate ranging from a low of 24.7 ksi/min (170 MPa/min) for Al to a high of 71.3 ksi/min (492 MPa/min) for SS304. The material properties calculated from the tensile tests are reported in Table 1.

2.2 Indentation Testing

A standard Rockwell hardness tester was used to measure the indentation hardness of the eight materials on the Rockwell B scale. Five tests were performed on each sample, for three samples per material. The summary results of the indentation tests are provided in Table 2.

The AnCu was too soft for measuring the hardness via an indentation test. In what follows, the hardness of the AnCu is assumed to be a factor of 2.8 times the yield strength, then converted into the units of Brinell Hardness (kgf/mm^2), which gives a Brinell Hardness value of HB = 11.06. This assumption is based on the experimental work and theories developed by Tabor [28].

2.3 Strain Hardending Exponents

In what follows, the model used for comparison of the experimental results to numerical predictions requires a value for Meyer's Hardness exponent, which is indicative of the strain hardening characteristics of the material. As this quantity was not measured with high confidence, it is assumed to be 2.2 for all materials. In several cases, this assumption is revised based off of material data sheets from MatWeb, and is noted for each result. These values could be deduced from the results of calibrating the numerical model to the experimental data; however, this would introduce epistemic uncertainty into the

Material	Modulus (GPa)	Yield Strength (MPa)	Ultimate Strength (MPa)
6061 Aluminum	71.47	353.70	375.70
Annealed Copper	102.76	38.75	218.65
Copper*	117.2	68.9	—
Hiperco	225.69	208.91	392.08
Nitronic 60	171.03	357.37	713.53
Phosphor Bronze	99.23	370.25	399.21
Stainless Steel 304	187.02	331.72	713.54
Titanium*	116.00	480.00	—

Table 1. Material properties from tensile tests. *: Note that the tensile test data for both Copper and Titanium was unavailable at the time of publication, and the material properties are provided by the stock manufacturer.

Material	Average Hardness, Rockwell B	Average Hardness, Brinell	Standard Deviation, Brinell
6061 Aluminum	59.49	99.36	2.06
Annealed Copper*	—	—	—
Copper	44.03	86.76	0.74
Hiperco	95.14	211.14	5.25
Nitronic 60	90.25	186.93	5.59
Phosphor Bronze	81.63	158.80	8.78
Stainless Steel 304	93.36	206.91	18.33
Titanium	109.26	230.16	3.53

Table 2. Measured indentation hardness for the specimen. *: Note that no hardness value was measured for the Annealed Copper due to it being too soft for the indentation machine used.

values reported and is thus not done in the present analysis.

3 Coefficient of Restitution Experiments

A pendulum-based setup was chosen for the COR study in order to provide a high degree of resolution in impact velocities. With a long enough pendulum arm, effective drop heights (i.e. the equivalent of a vertical drop experiment) of less than a millimeter are possible, whereas such small drops would be difficult with a vertical drop experiment. For instance, in [15], drops from a height of no less than 25 mm were able to be measured accurately. One challenge that existed with the pendulum method, though, was minimizing the out-of-plane motion of the pendulum due to effects such as air currents within the lab, imperfect releases, etc. To address this, a sliding stage test stand was utilized, as detailed below, and a vacuum chuck powered by a compressor was used to minimize rotational motion upon release of the sphere for a test.

3.1 Pendulum Details

The longest pendulum achievable within the laboratory had an arm length of 2.189 m, which produces a pendulum with a period of approximately three seconds (Fig. 2). For comparison, the pendulums used in [17] are less than 40 cm in length. With a pendulum that is 2.189 m long, small horizontal displacements of the release point allow for a high degree of resolution in changing the impact velocities.

The pendulum itself consists of a 440c Grade 100 Wear Resistant Stainless Steel (hereafter referred to as 440c) sphere of radius 1.1125 cm that impacts the test specimen, and is attached to a support structure by a thin wire that is threaded through

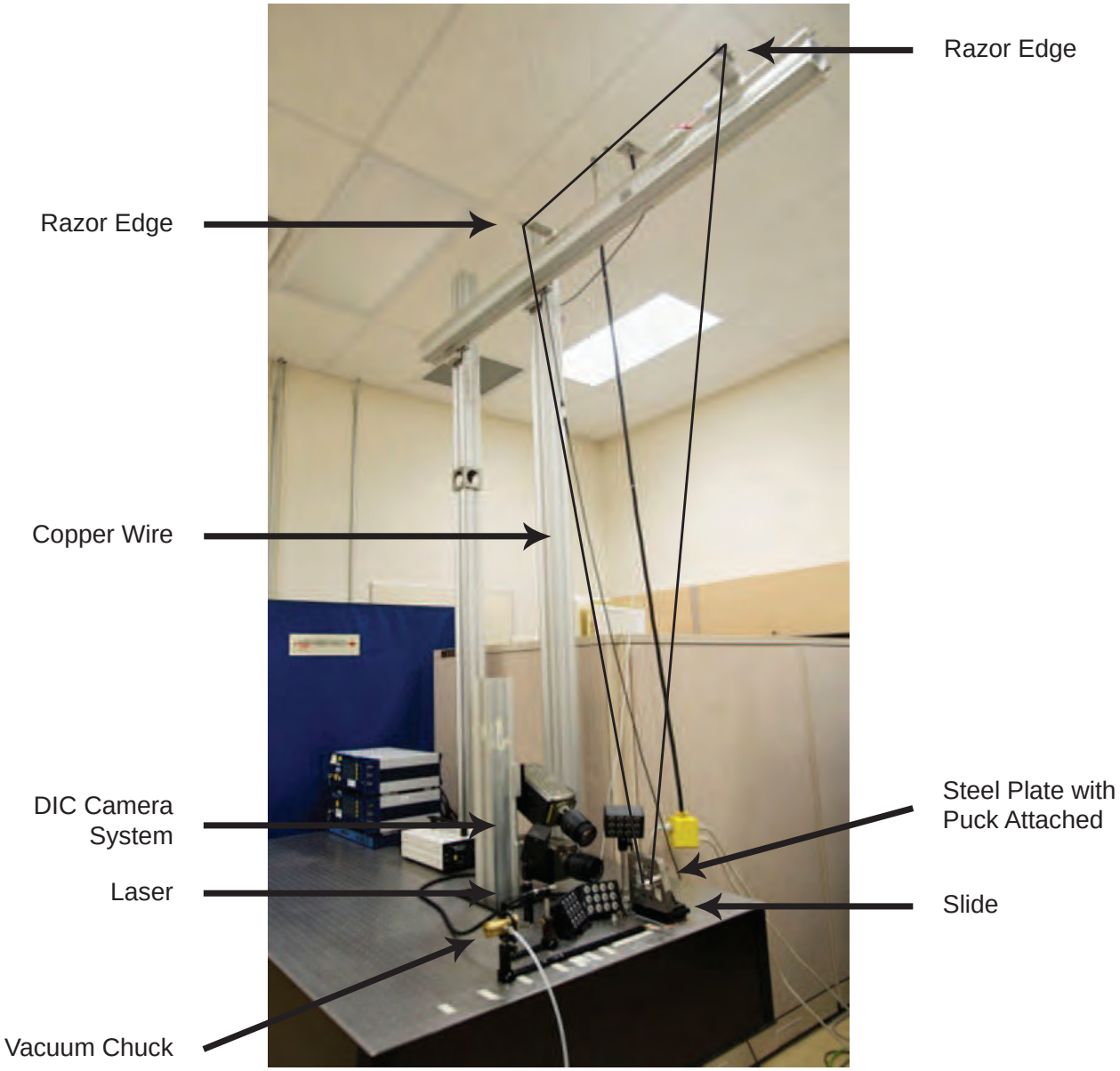

Fig. 2. Experimental setup for the pendulum-based COR tests.

a hole drilled into the center of the sphere (this wire is highlighted by black lines in Fig. 2 to make it visible). Assumed properties for the 440c sphere are given in Table 3. To minimize frictional losses, the pendulum wire is supported by razor edges. By having the wire setup to support the sphere at two point, this was found to help reduce out-of-plane motion. Additionally, as the wires are made out of copper, it was possible to construct an electrical circuit from the wires through the sphere to the test specimen to measure contact duration.

3.1.1 Specimen Mounting

The first generation of the test stand involved the specimen being attached to a large mass such that $m_f \gg m_s$ (with m_f being the mass of the specimen and fixture, and m_s being the mass of the sphere). While this setup provides consistent data, early versions of it exhibited out-of-plane motion for the highest impact velocities that caused error in the calculation of the COR. Thus, a sliding stage was introduced such that the sphere can swing freely for a number of periods in order to dissipate out-of-plane motion. As shown in Fig. 3, the puck was mounted on a steel plate that was fastened to an L-Bracket attached to a crossed-roller bearing stage. Immediately before an impact, the stage was able to be slid and locked into place, providing a rigid fixture. To assess this assumption of rigidity, laser Doppler vibrometry (LDV) was used to measure the motion of the fixture across an impact event. Results indicated that the assumption was valid as the motion of the fixture was near the noise threshold of the LDV.

Property	Value
Elastic Modulus	205 GPa
Poisson's Ratio	0.29
Density	7800 kg/m^3
Brinell Hardness	600 kgf/mm^2
Radius	1.1125 cm

Table 3. Assumed properties of the 440c Grade 100 Wear Resistant Stainless Steel sphere used in the COR experiments.

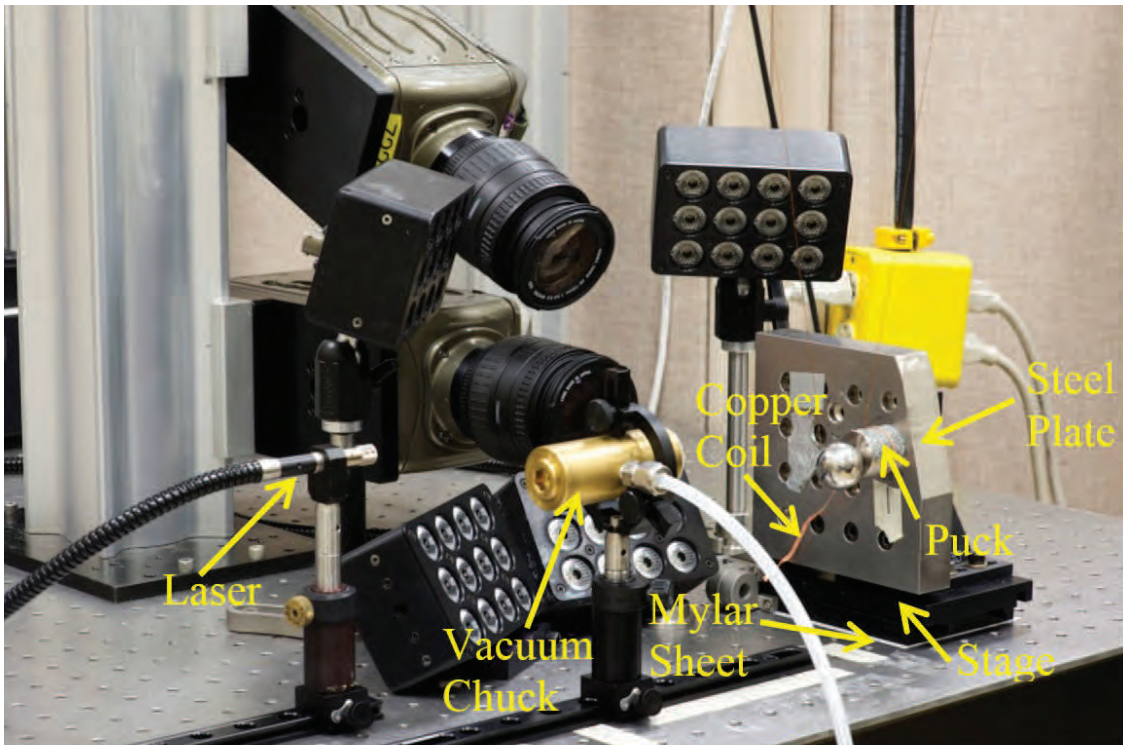

Fig. 3. Close-up of the impact location and the experimental setup for the COR experiments.

3.1.2 Data Acquisition

Data was acquired primarily through digital image correlation (DIC), though some data was also acquired through LDV to confirm the accuracy of the DIC measurements. Two Phantom v7 cameras were used in the DIC setup, providing framerates at 1000 frames per second (contrasted with the 30 frames/second resolution in [17, 19] and the stroboscopic approach used in [15, 18]). In order to provide illumination sufficient for the DIC method, four LED flood lights were used to evenly illuminate the sphere during its travel. For details about DIC, refer to [29–31].

Contact durations were recorded for each impact by passing a current through the pendulum wire, and recording this current on the block. The circuit was insulated from the table using a Mylar sheet between the stage holding the puck and the optical table and bolted down using nylon bolts. A copper coil is wrapped around the puck, so that the circuit is closed at the start of impact, and is opened at the end of impact. The circuit's current is recorded directly on the data acquisition device. Typical impact times are on the order of 100 micro-seconds, too short to record in high resolution using the DIC cameras, but within the accuracy of the acquisition hardware.

3.2 Measured Coefficients of Restitution and Impact Times

The results for the eight materials tested are displayed here both in terms of the COR and the contact durations (where available). The COR is experimentally measured as the ratio of the magnitude of the velocity of the sphere after an impact

to the magnitude of the velocity of the sphere before an impact. From the COR equations

$$v_s^+ = \frac{m_s v_s^- + m_f v_f^- + m_f e\left(v_f^- - v_s^-\right)}{m_s + m_f} \tag{1}$$

$$v_f^+ = \frac{m_s v_s^- + m_f v_f^- + m_s e\left(v_s^- - v_f^-\right)}{m_s + m_f}, \tag{2}$$

where v^- indicates the velocity immediately before an impact, v^+ indicates the velocity immediately after an impact, e is the COR, and subscripts s and f indicate the sphere and fixture respectively. With $v_f^- = 0$,

$$v_s^+ \approx -e v_s^- \tag{3}$$

and

$$v_f^+ \approx 0 \tag{4}$$

for non-high speed impacts.

Each specimen is impacted only once at one of nine locations on its surface, ensuring that no residual effects from previous tests were present. Thus, multiple specimen of each material were used in the experiments. As the slide method was implemented part way through the experimental testing, it is noted throughout when the slide method was used to gather the data. Additionally, for the COR study, comparisons are made to the model of [6] to highlight the trends observed in the data.

3.2.1 Aluminum 6061

All 12 drop heights[3] were tested without using the slide stage; impact was directly after release. Overall, the model [6] slightly over-predicts the measured COR (Fig. 4) and underpredicts the contact duration (Fig. 5), but accurately predicts the trends observed in the data. A Meyer's Hardness of 2.2 was assumed for the predictions.

3.2.2 Annealed Copper

All nine drop heights were tested using the slide stage. Impact occurred after the ball swung for approximately five minutes. Excellent agreement between the measurements and the model [6] was observed, as shown in Fig. 6. A Meyer's Hardness of 2.2 was assumed for the predictions. No data for the contact duration is available.

3.2.3 Copper

In order to demonstrate the effects of heat treating on the dissipation characteristics of common metals, a small number of experiments on the Cu pucks that were not annealed were performed. Four drop heights were tested using the slide stage. Impact was after the ball swung for approximately five minutes. Good agreement between the measurements and the model [6] were observed. A Meyer's Hardness of 2.1 was assumed for the predictions. No data for the contact duration is available.

3.2.4 Hiperco

All nine drop heights were tested using the slide stage. Impact occurred after approximately five minutes. Excellent agreement is observed between the measurements and the model [6] for both CORs (Fig. 8) and contact durations (Fig. 9). A Meyer's Hardness of 2.1 was assumed for the predictions.

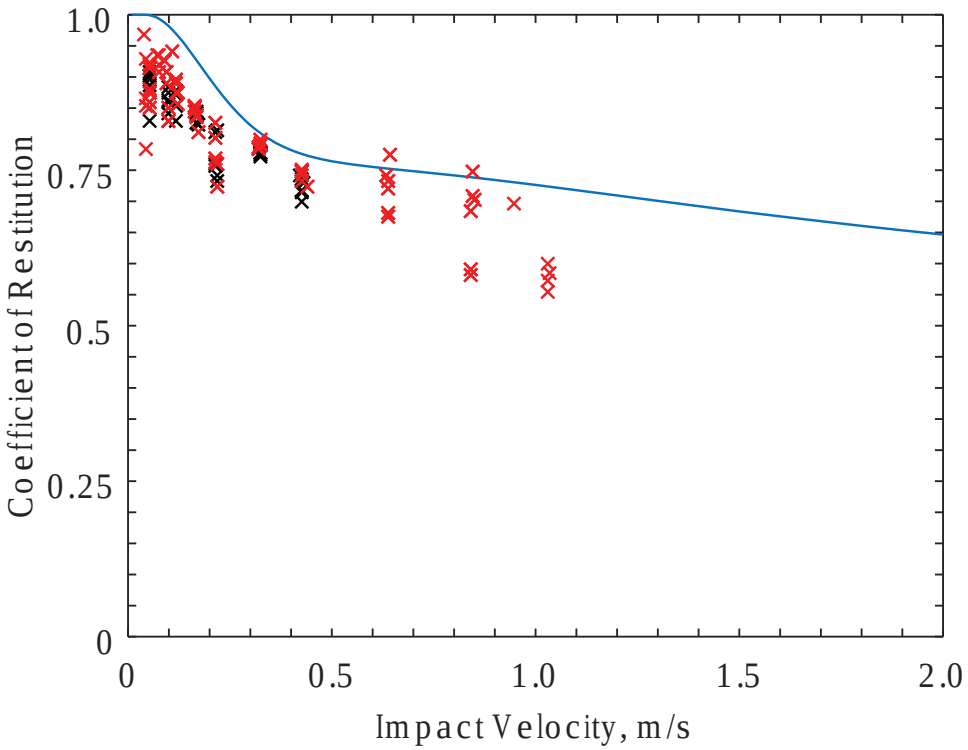

Fig. 4. Aluminum 6061 measured COR. Red x: DIC; Black : LDV; Blue curve: [6].

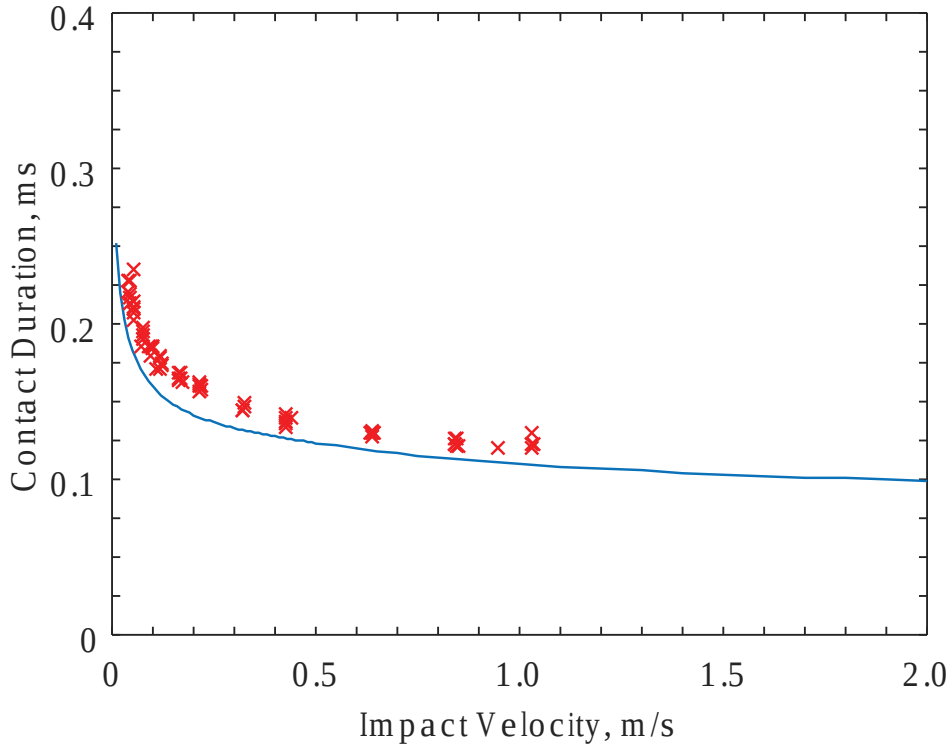

Fig. 5. Aluminum 6061 measured contact times. Red x: measurement; Blue curve: [6].

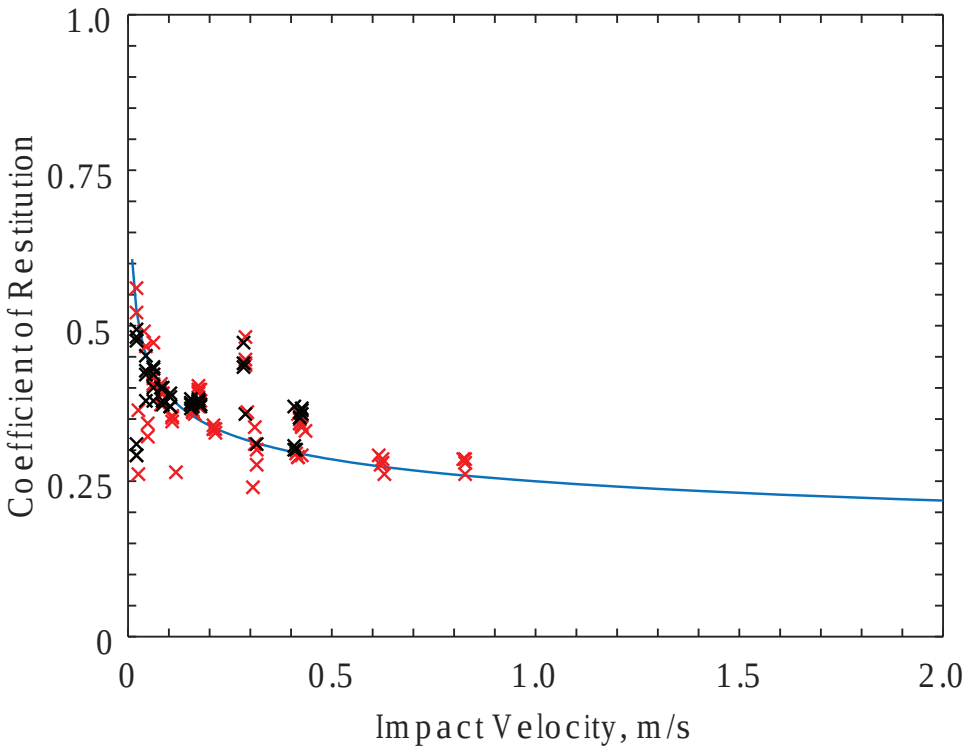

Fig. 6. Annealed Copper measured COR. Red x: DIC; Black x: LDV; Blue curve: [6].

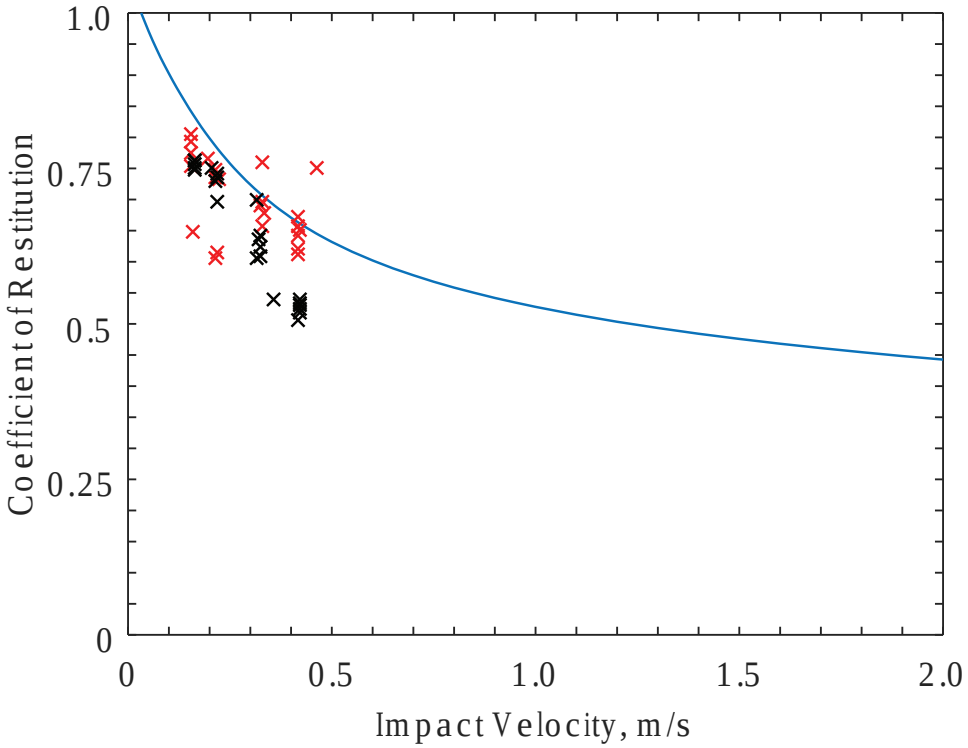

Fig. 7. Copper measured COR. Red x: DIC; Black x: LDV; Blue curve: [6].

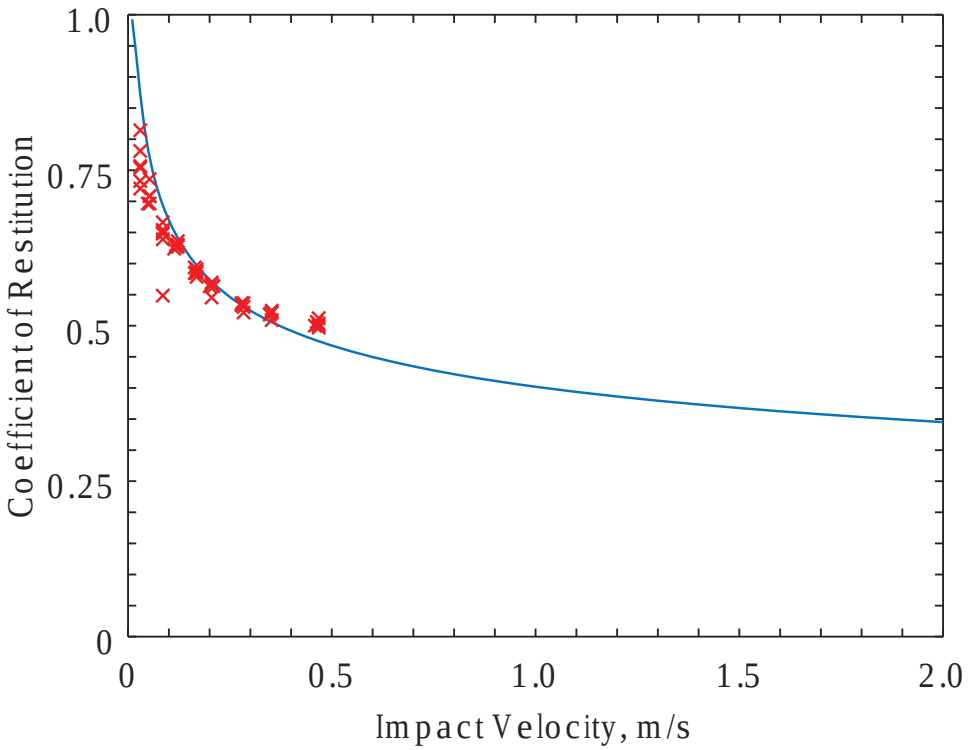

Fig. 8. Hiperco measured COR. Red x: DIC; Black x: LDV; Blue curve: [6].

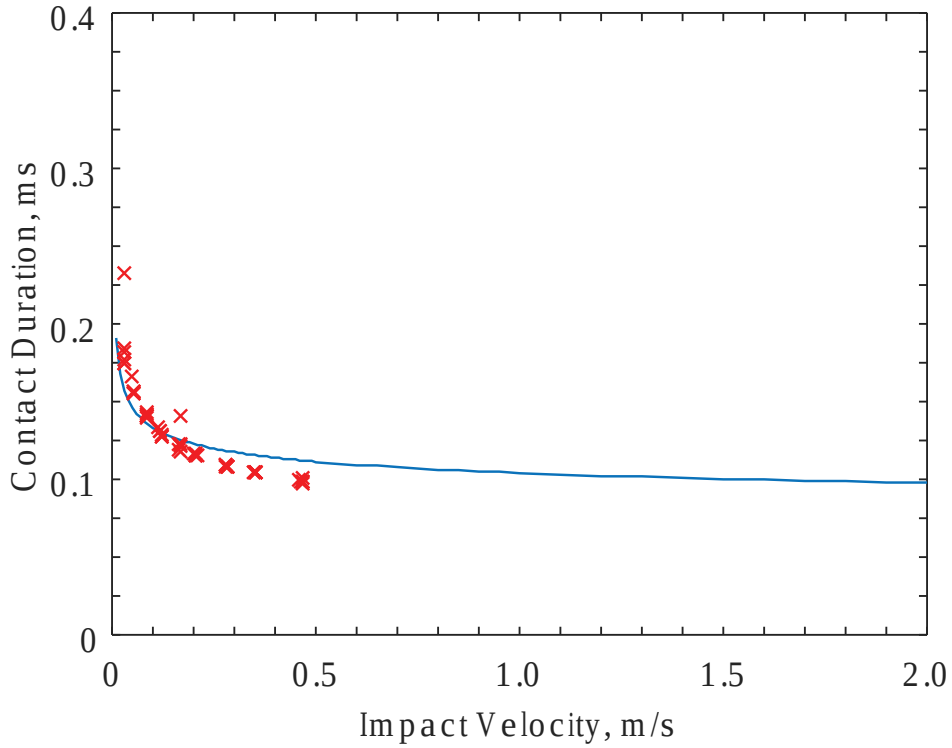

Fig. 9. Hiperco measured contact times. Red x: measurement; Blue curve: [6].

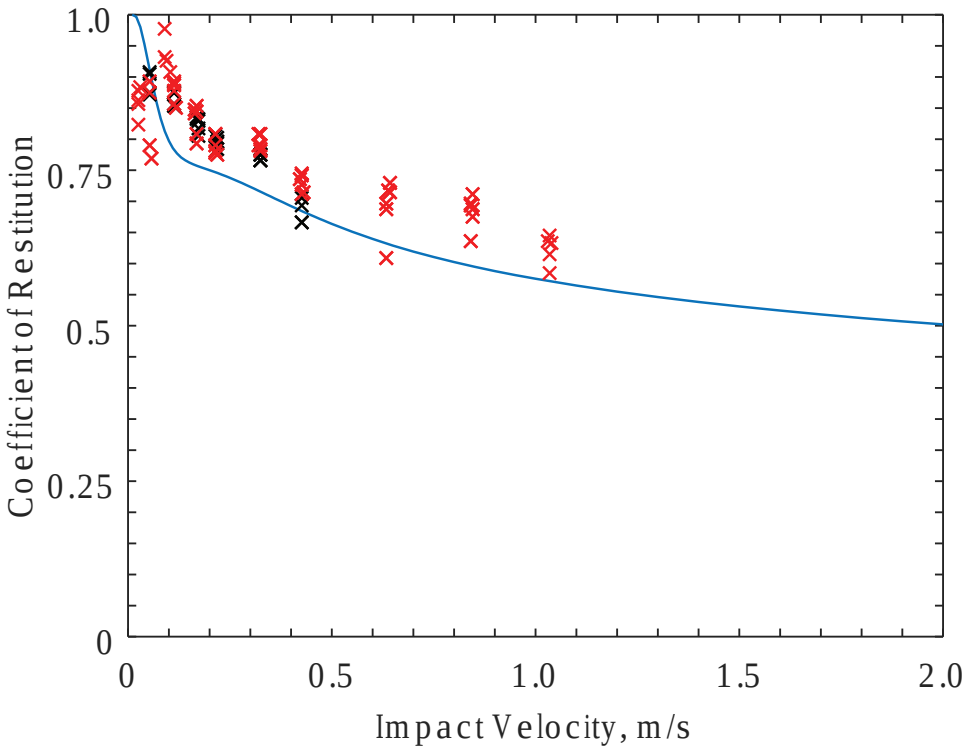

Fig. 10. Nitronic 60A measured COR. Red x: DIC; Black x: LDV; Blue curve: [6].

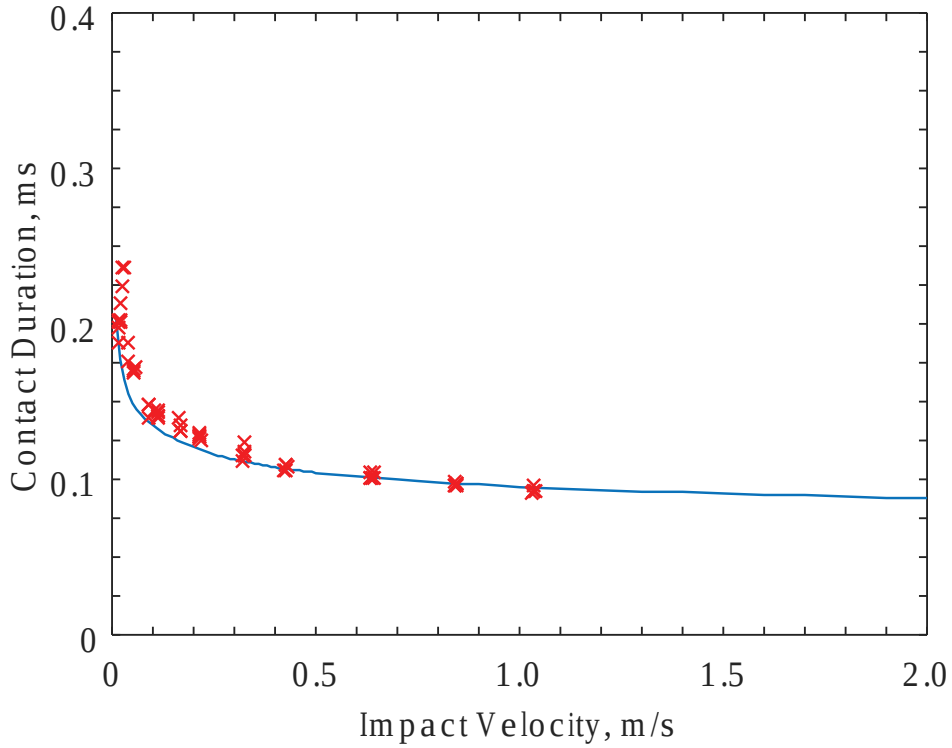

Fig. 11. Nitronic 60A measured contact times. Red x: measurement; Blue curve: [6].

3.2.5 Nitronic 60A

All 11 drop heights were tested without the slide stage. The COR data near 10 mm/s was not consistent and an additional 13 tests were conducted about impact velocities of 10 mm/s using the slide (Fig. 10). Good agreement between the model [6] and measurements was observed, especially for the contact times (Fig. 11). A Meyer's Hardness of 2.2 was assumed for the predictions.

3.2.6 Phosphor Bronze

All 11 drop heights were tested without the slide stage; impact was directly after release. Overall, the trends of the measurements and model [6] agree in Figs. 12 and 13, though the model over-predicts the COR (Fig. 12). This is partly attributable to the large specimen-to-specimen variability observed in terms of mechanical properties; the standard deviation of the Brinell Hardness is 9 kgf/mm^2, the standard deviation of the Elastic modulus is 19 GPa, and the standard deviation of the yield strength is 10 MPa. A Meyer's Hardness of 2.2 was assumed for the predictions.

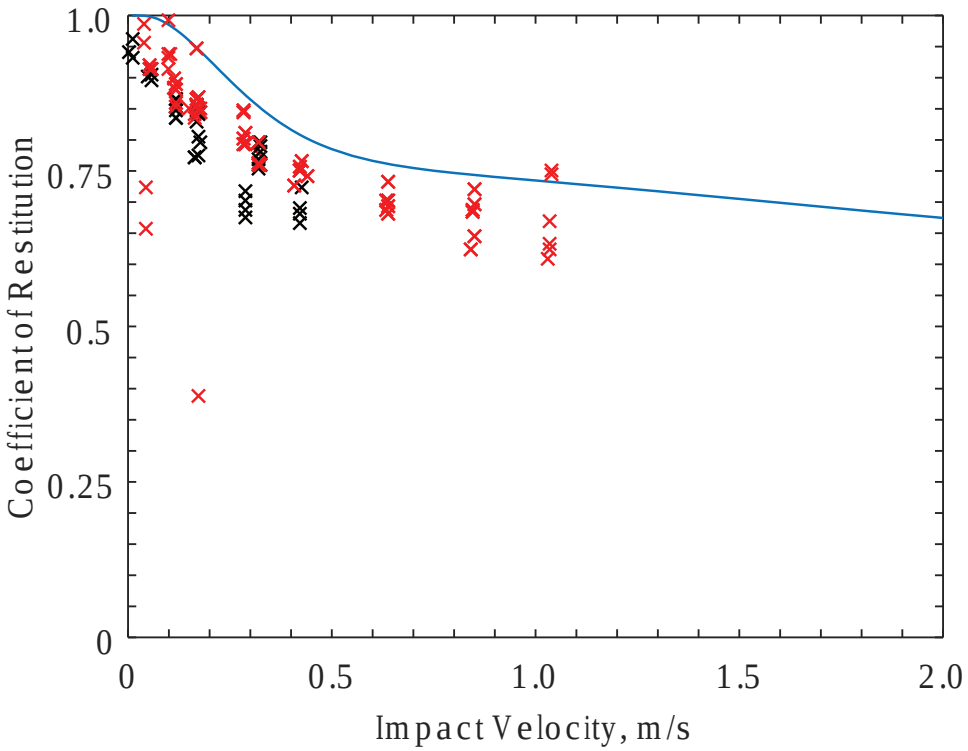

Fig. 12. Phosphor Bronze measured COR. Red x: DIC; Black x: LDV; Blue curve: [6].

3.2.7 Stainless Steel 304

All 11 drop heights were originally tested without using the slide stage. The data for impact velocities near 10 mm/s were not consistent; therefore an additional 12 tests were conducted using the slide stage with the results reported in Fig. 14. Excellent agreement is observed between the experiments and the model [6], though the contact times (Fig. 15) are slightly under-predicted. A Meyer's Hardness of 2.25 was assumed for the predictions.

3.2.8 Titanium

All eight drop heights were tested using the slide stage. Impact was after the ball swung for approximatley five minutes. For the COR measurements, the model [6] significantly over-predicts the measuremed CORs (Fig. 16), and slightly under-predicts the contact times (Fig. 17). This is most likely due to incorrect material properties as the values in Table 1 are provided and not measured. A Meyer's Hardness of 2.2 was assumed for the predictions.

---

[3] Note, multiple tests are conducted at each drop height.

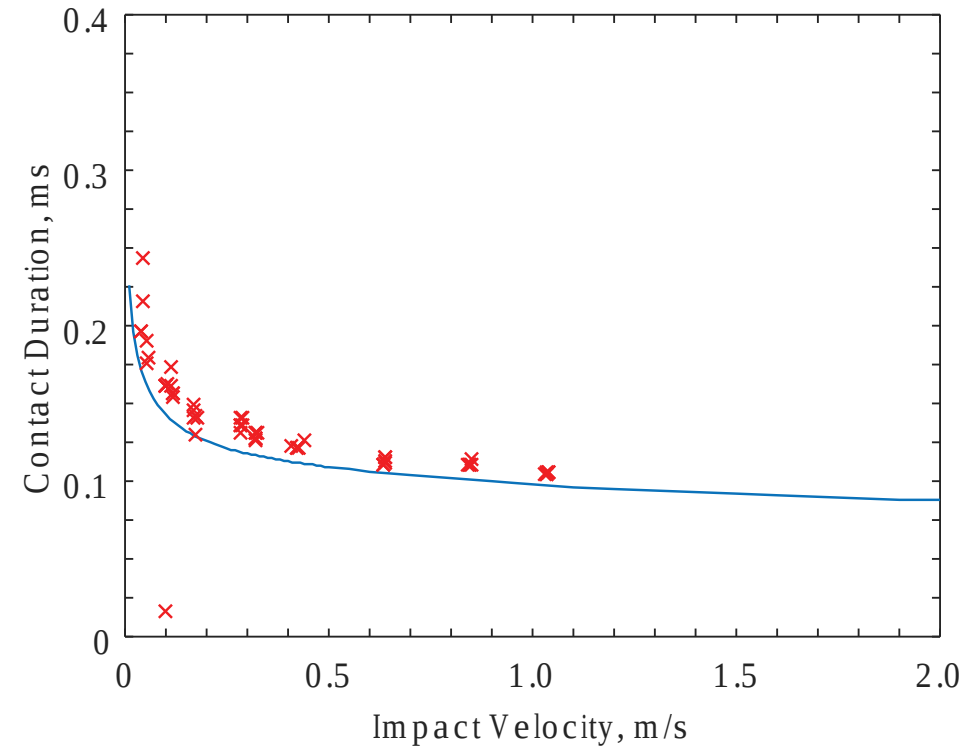

Fig. 13. Phosphor Bronce measured contact times. Red x: measurement; Blue curve: [6].

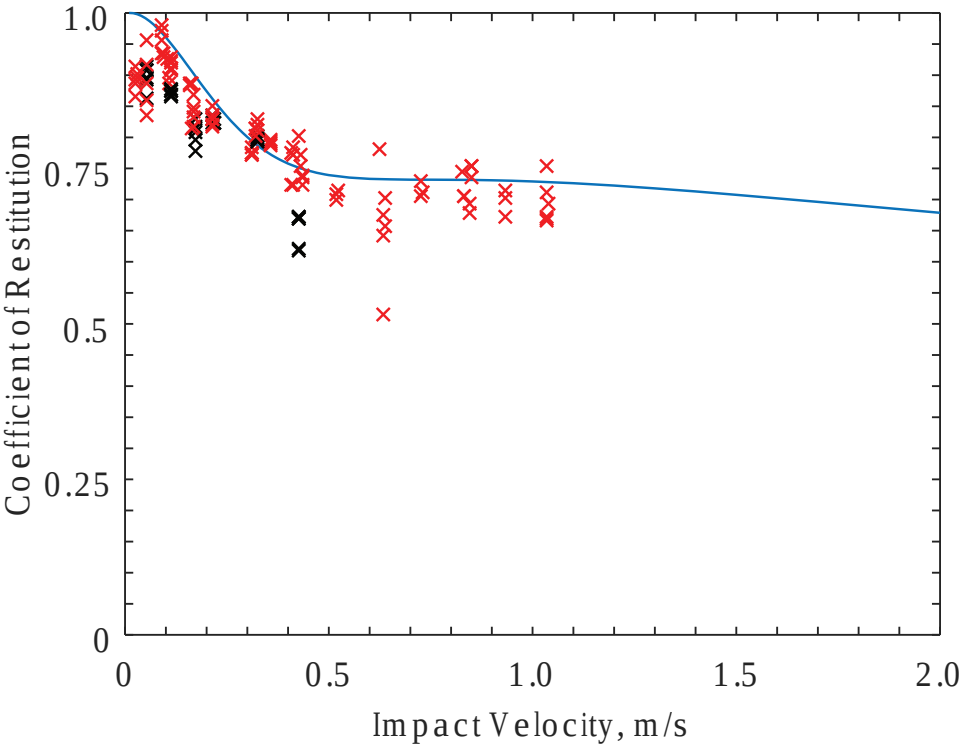

Fig. 14. Stainless Steel 304 measured COR. Red x: DIC; Black x: LDV; Blue curve: [6].

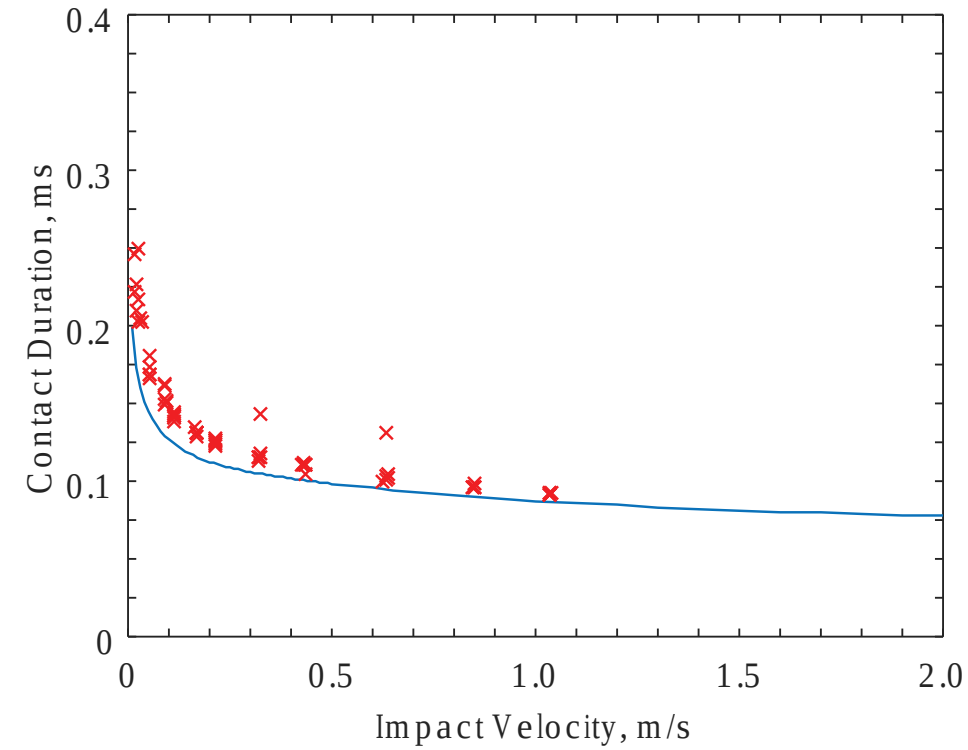

Fig. 15. Stainless Steel 304 measured contact times. Red x: measurement; Blue curve: [6].

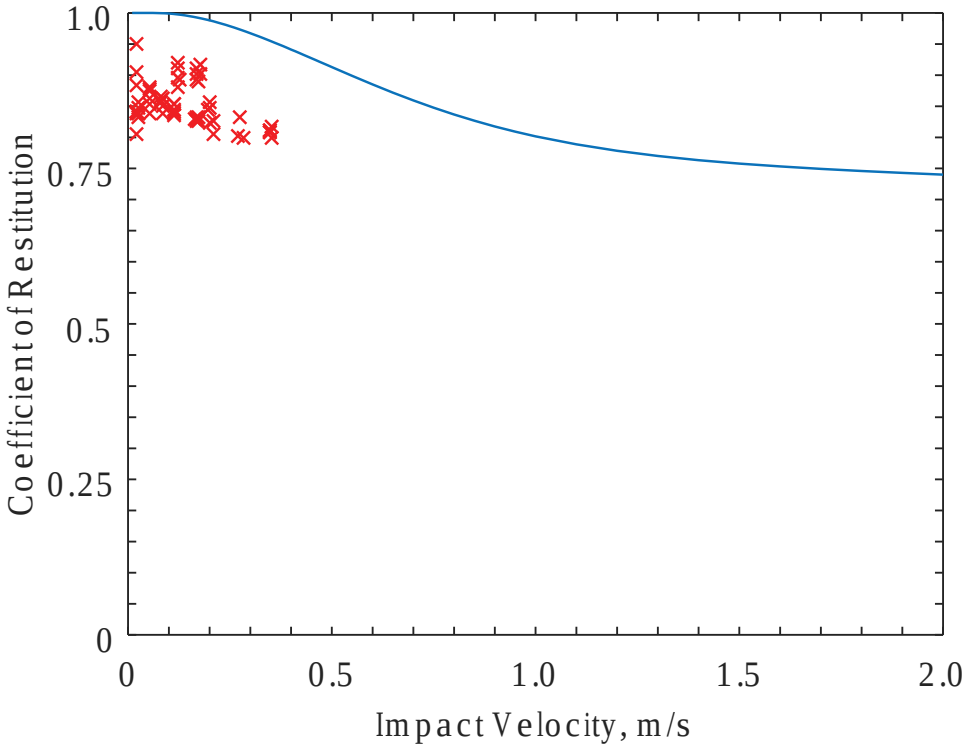

Fig. 16. Titanium measured COR. Red x: DIC; Black x: LDV; Blue curve: [6].

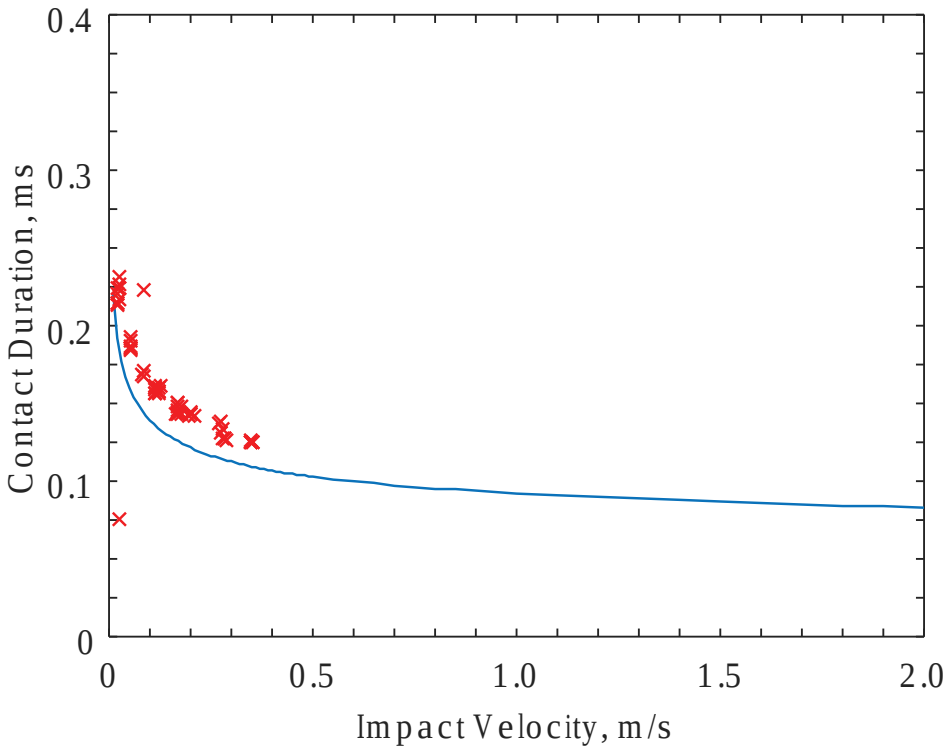

Fig. 17. Titanium measured contact times. Red x: measurement; Blue curve: [6].

4 Compliance Measurements

In contrast to the COR measurements, which ultimately provide only two data points (the COR and contact duration) for each impact, the compliance measurements result in high resolution force-displacement curves for each contact test.

4.1 Micro- and Nano-Indentation Machines

Characterization of all samples was performed using micro- and nano-indentation machines [32], shown in Fig. 18. The micro- and nano-indentation machines were designed to measure the compliance and hardness of samples with accuracy on the order of approximately one nm in displacement and 0.1 mN in force (the measured noise threshold of the device was on the order of 10 μN and 0.01 nm). The measurements were made using an indenter fixed to the end of a pendulum, which was actuated using a voice coil motor to impact the sample a single time before being recaptured by the electromagnetic forces from the voice coil motor. The samples themselves were held on a robotic stage (Fig. 19), which lets the system be automated to allow for batches of experiments to be queued, resulting in a large number of measurements being made in order to quantify the uncertainty and variability in the measurements.

Each sample indentation had a 30 second load and unload time with a five second dwell at the maximum load, and a 30 second dwell at 90% unload in order to quantify the thermal drift in the measurements. The raw data exhibited inconsistencies due to thermal drifts, and was also convoluted by the compliance of the machine fixture. For these reasons, it was necessary to apply corrections to the raw data.

4.1.1 Data Corrections

Indentation curves were not included in the results if their maximum displacement was more than two standard deviations from the mean of the maximum displacement of corresponding indentations. A scaling factor was applied to the raw displacement values to correct the force inconsistency due to the compliance of the two fixtures being convoluted with the measurements. In effect, the scaling factor ensured that the slope of the data at low displacement values was approximately the same across all measurements, as is expected. The data for the 250 mN peak load experiments was used as the reference data as these measurements were conducted on both the micro-indenter and nano-indenter and were closest to the theoretical predictions of [6]. The scaling constant was determined from calibration experiments for each indenter, and more details can be found in [32].

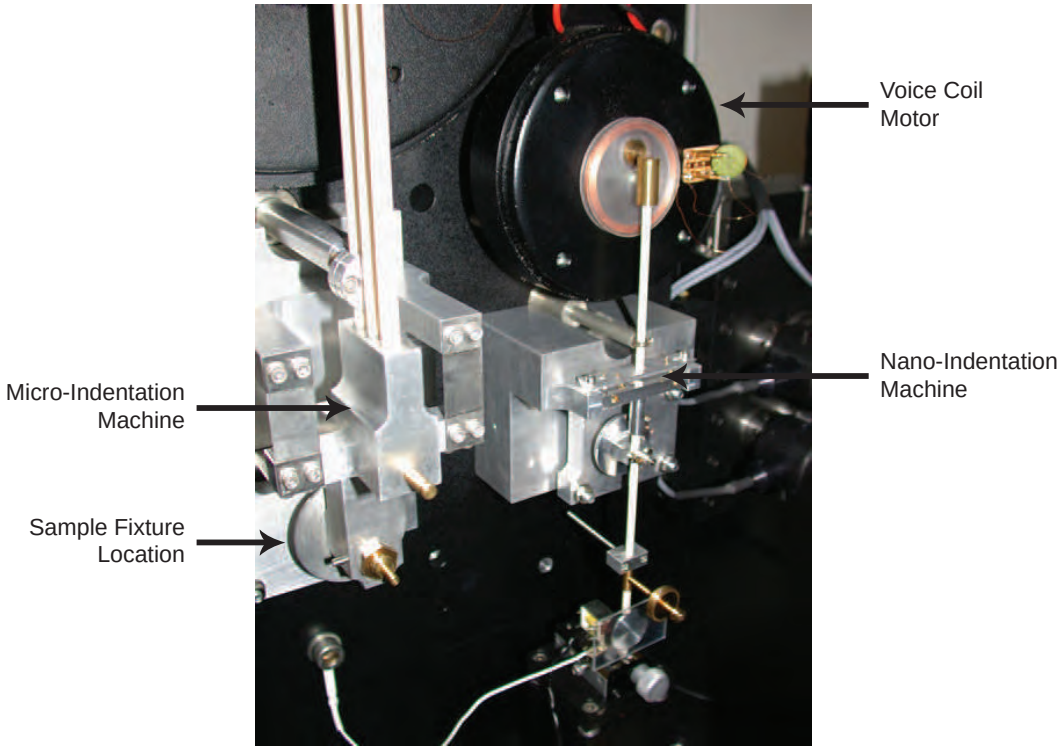

Fig. 18. Close-up view of the micro- and nano-indentation machines.

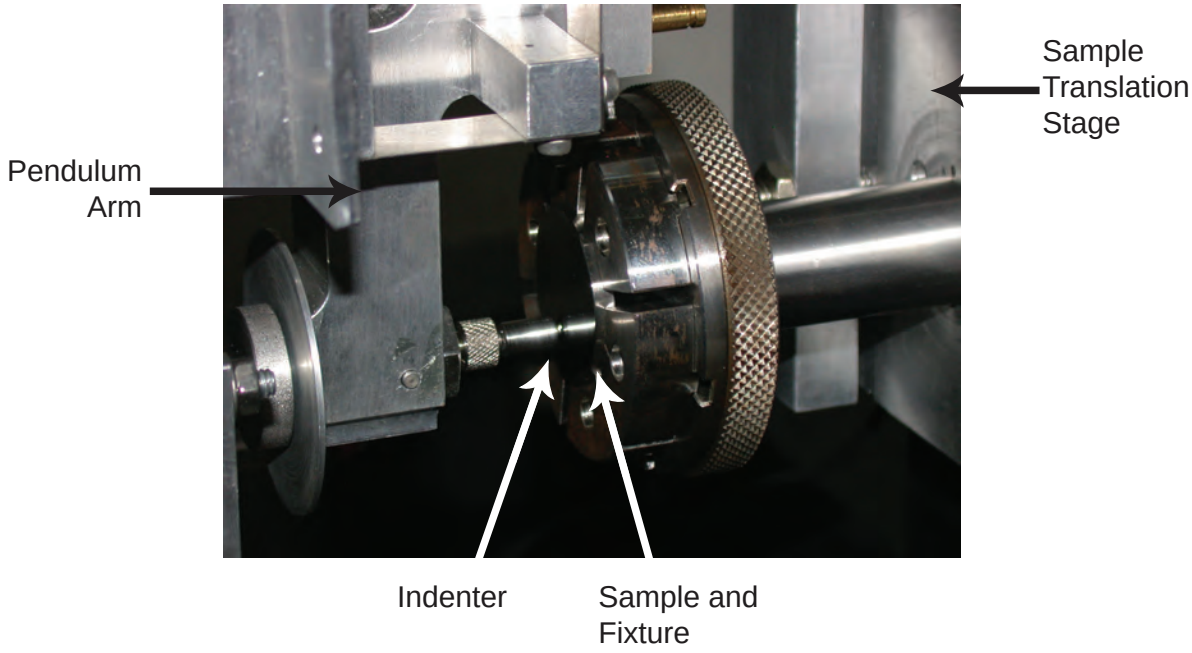

Fig. 19. View of the sample and fixture within the micro-indentation machine.

4.1.2 Indenters

Two different indenters were used for measuring the compliance curves: a 440c indenter of diameter 3.175 mm, and a Sapphire indenter of diameter 3.155 mm. These two indenters were chosen in order to assess the effects of the indenter hardness on the measurement conditions. Typically, the indenter was assumed to be rigid as its hardness was orders of magnitude greater than the test specimen; however, recent research has demonstrated that the hardness of the indenter affects the measured compliance curves [6]. The material properties of the 440c indenter are given in Table 3, and the properties of

the Sapphire indenter are given in Table 4

Property	**Value**
Elastic Modulus	370 GPa
Poisson's Ratio	0.22
Density	3980 kg/m^3
Brinell Hardness	1740 kgf/mm^2

Table 4. Assumed properties of the Sapphire sphere used in the compliance experiments.

4.2 Measured Force-Displacement Compliance Data

The results for the eight materials tested are reported here for indentation via both the 440c sphere and the Sapphire sphere. For all samples, six load levels were used: 25 mN, 100 mN, 250 mN, 1 N, 5 N and 10 N. To assess the uncertainty in the measurements, nine indentations were made at each load level for each sample. Due to the large volume of data collected, comparisons to models are omitted for the compliance study in order to focus solely on the measurements. For comparisons to a subset of this data, refer to [6].

4.2.1 Aluminum 6061

The compliance measurements for the Al samples are shown in Fig. 20 for indentation via the 440c sphere, and Fig. 21 for indentation via the Sapphire sphere. For the 440c sphere results, evidence of thermal drift at the 90% unload point is evident in one of the measurements at the lowest load tested (Fig. 20(a)). As well, evidence of thermal drift at the peak load is observed in several of the tests at the highest load tested (Fig. 20(f)). Results for both the 440c sphere and Sapphire sphere are shown to be very repeatable.

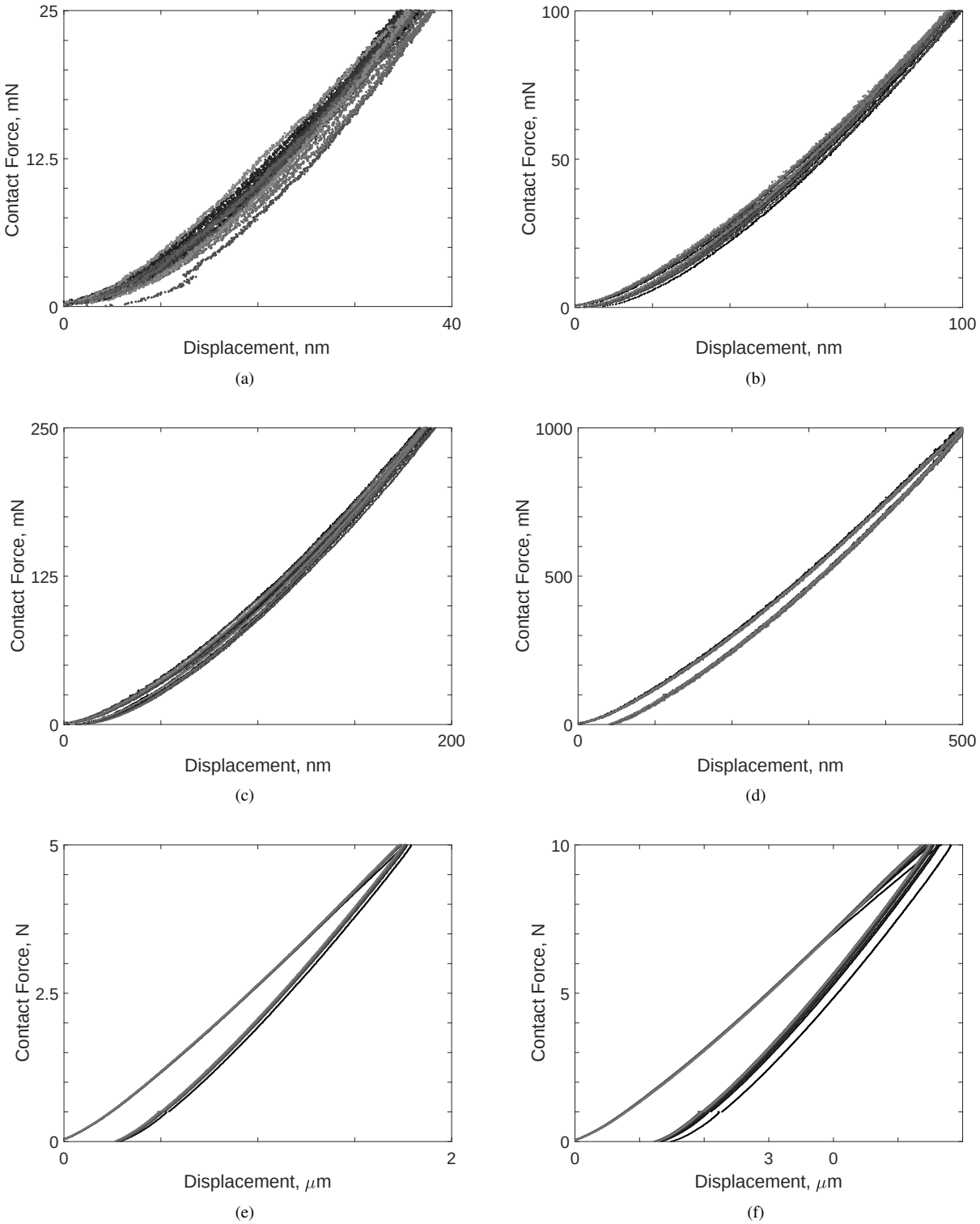

Fig. 20. Compliance measurements of 6061 Aluminum indented by the 440c Grade 100 Wear Resistant Stainless Steel sphere for peak loads of (a) 25 mN, (b) 100 mN, (c) 250 mN, (d) 1 N, (e) 5 N, and (f) 10 N. Each load has nine separate measurements.

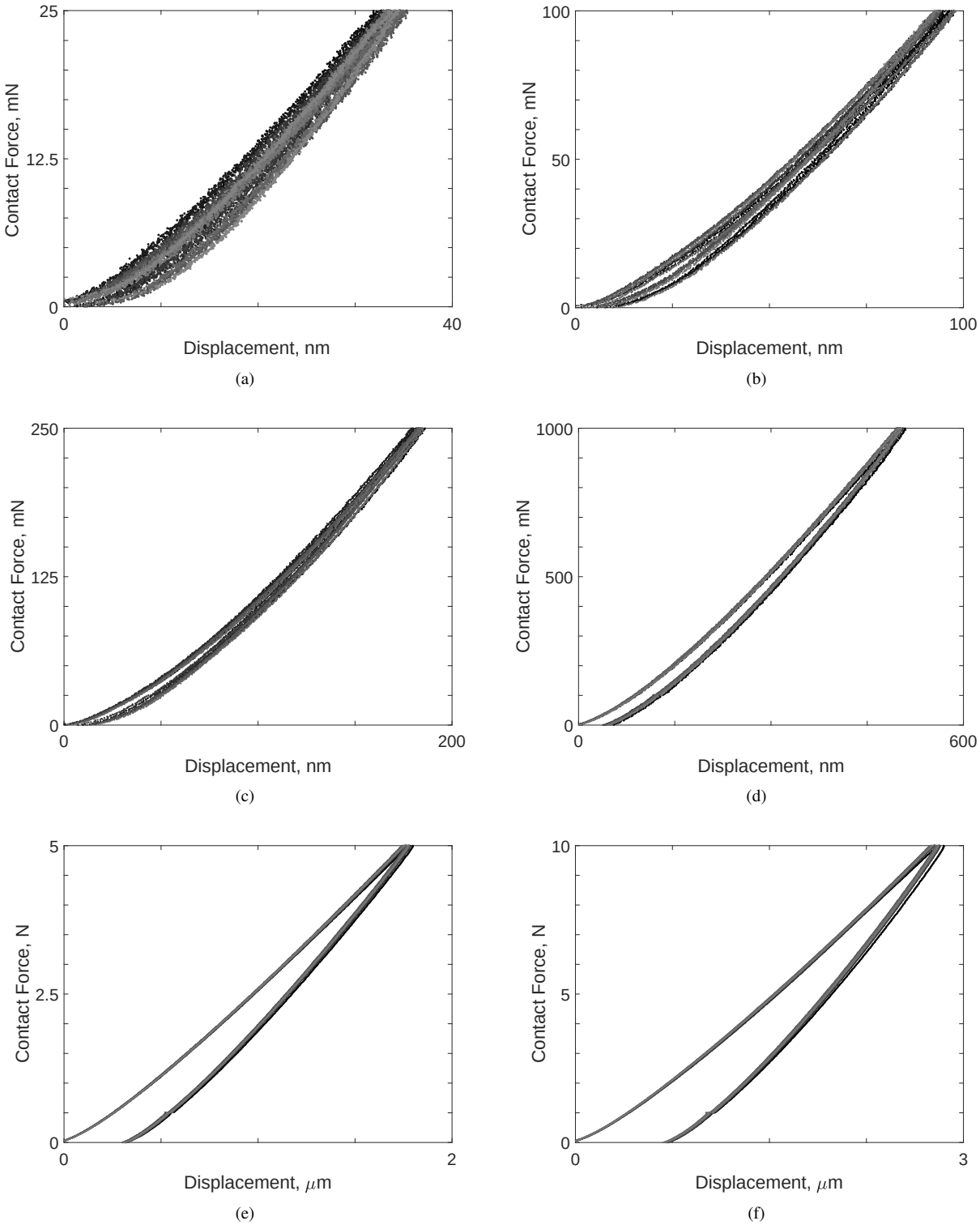

Fig. 21. Compliance measurements of 6061 Aluminum indented by the Sapphire sphere for peak loads of (a) 25 mN, (b) 100 mN, (c) 250 mN, (d) 1 N, (e) 5 N, and (f) 10 N. Each load has nine separate measurements.

4.2.2 Annealed Copper

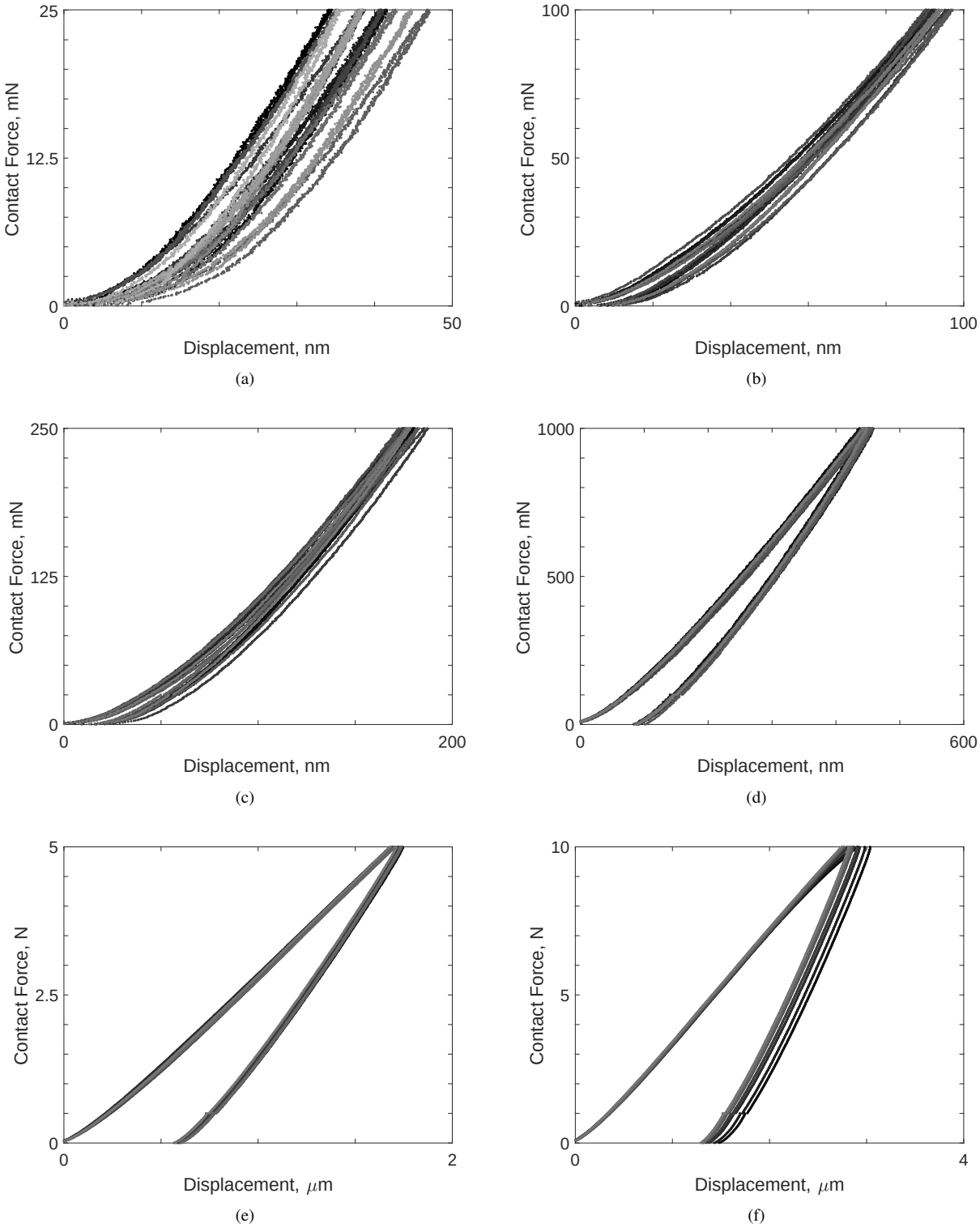

Fig. 22. Compliance measurements of Annealed Copper indented by the 440c Grade 100 Wear Resistant Stainless Steel sphere for peak loads of (a) 25 mN, (b) 100 mN, (c) 250 mN, (d) 1 N, (e) 5 N, and (f) 10 N. Each load has nine separate measurements.

The compliance measurements for the AnCu samples are shown in Fig. 22 for indentation via the 440c sphere, and

Fig. 23 for indentation via the Sapphire sphere. Significant variation is observed in the low load tests with the 440c sphere, particularly at the lowest load (Fig. 22(a)). Less variation is observed in the Sapphire sphere measurements at low loads; however, significantly higher variation is observed at high loads, particularly at the highest load tested (Fig. 23(f)). This is, perhaps, due to thermal drift issues during testing.

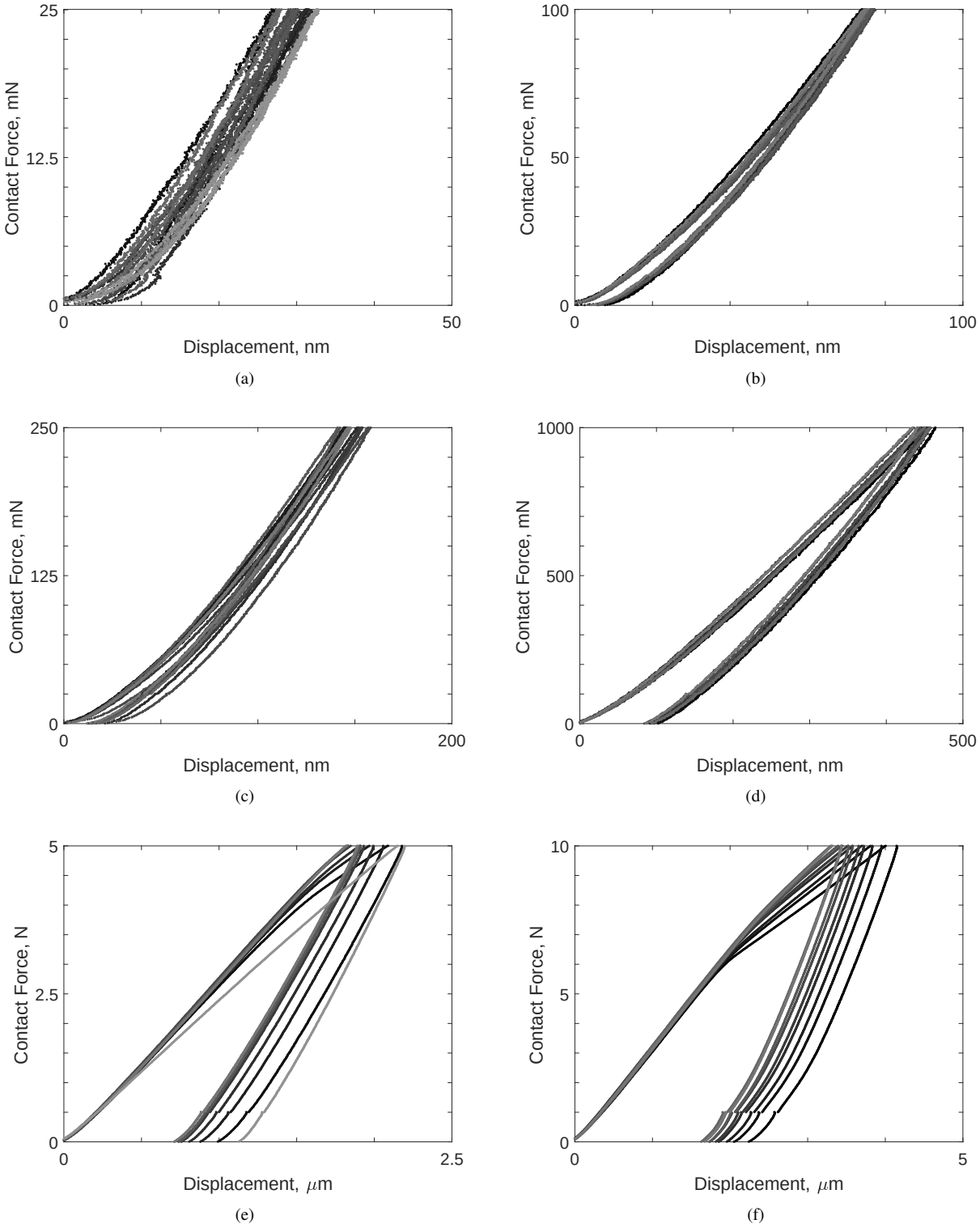

Fig. 23. Compliance measurements of Annealed Copper indented by the Sapphire sphere for peak loads of (a) 25 mN, (b) 100 mN, (c) 250 mN, (d) 1 N, (e) 5 N, and (f) 10 N. Each load has nine separate measurements.

4.2.3 Copper

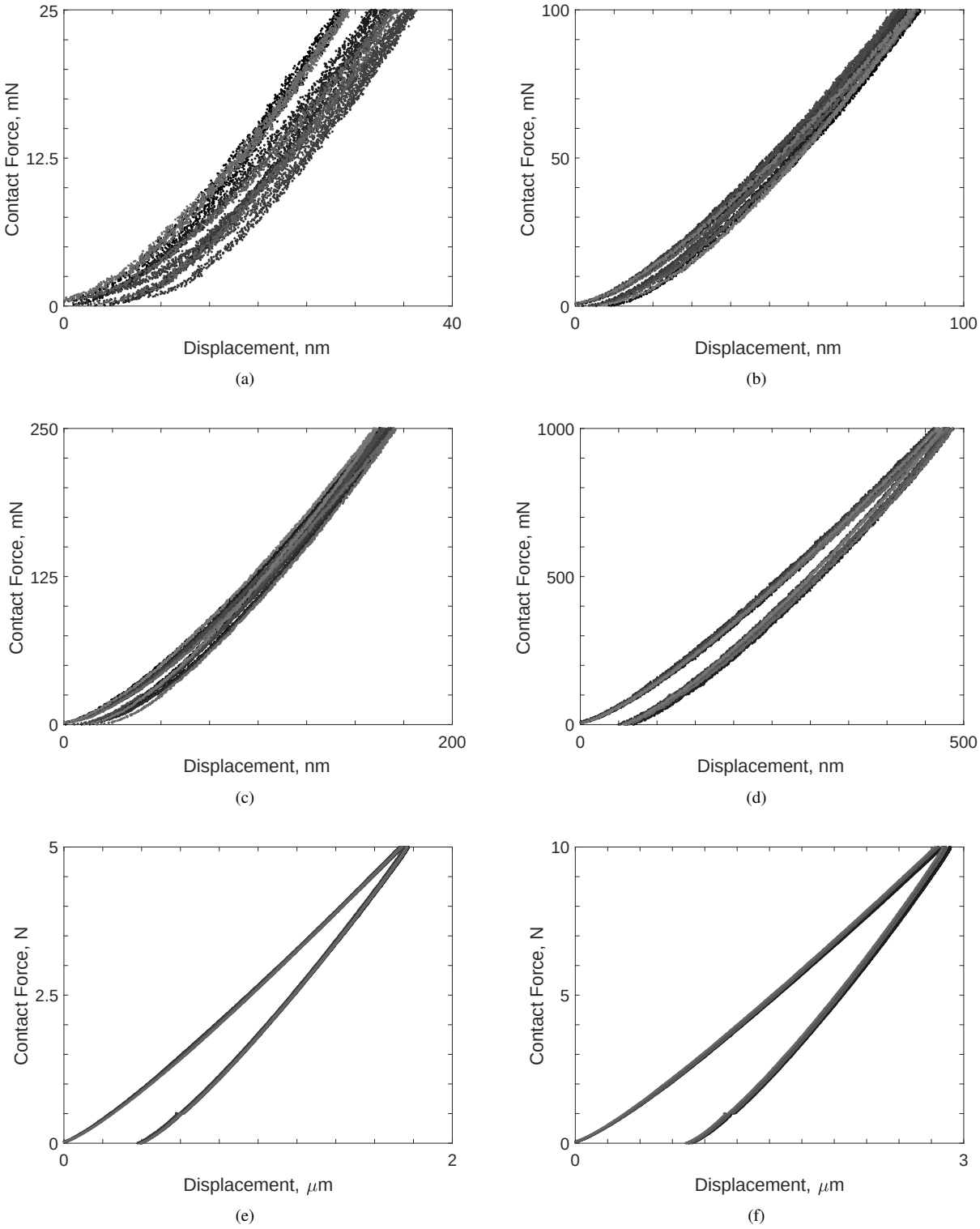

Fig. 24. Compliance measurements of Copper indented by the 440c Grade 100 Wear Resistant Stainless Steel sphere for peak loads of (a) 25 mN, (b) 100 mN, (c) 250 mN, (d) 1 N, (e) 5 N, and (f) 10 N. Each load has nine separate measurements.

The compliance measurements for the Cu samples are shown in Fig. 24 for indentation via the 440c sphere, and Fig. 25

for indentation via the Sapphire sphere. A similar trend as for the AnCu samples is observed: higher variability is observed in the low peak force measurements for the 440c spheres compared to the Sapphire spheres, and lower variability is observed for the high peak force measurements of the 440c spheres compared to the Sapphire spheres.

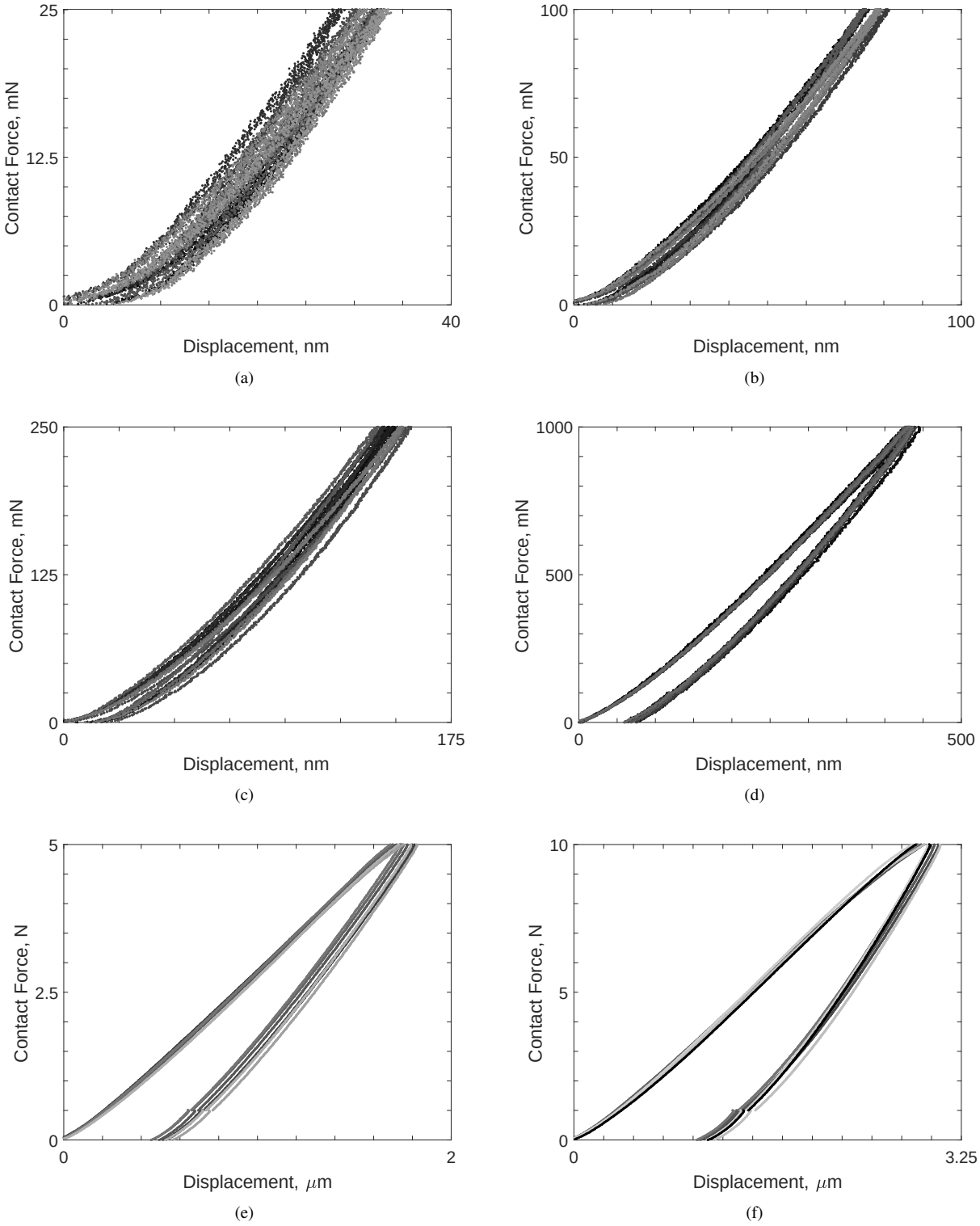

Fig. 25. Compliance measurements of Copper indented by the Sapphire sphere for peak loads of (a) 25 mN, (b) 100 mN, (c) 250 mN, (d) 1 N, (e) 5 N, and (f) 10 N. Each load has nine separate measurements.

4.2.4 Hiperco

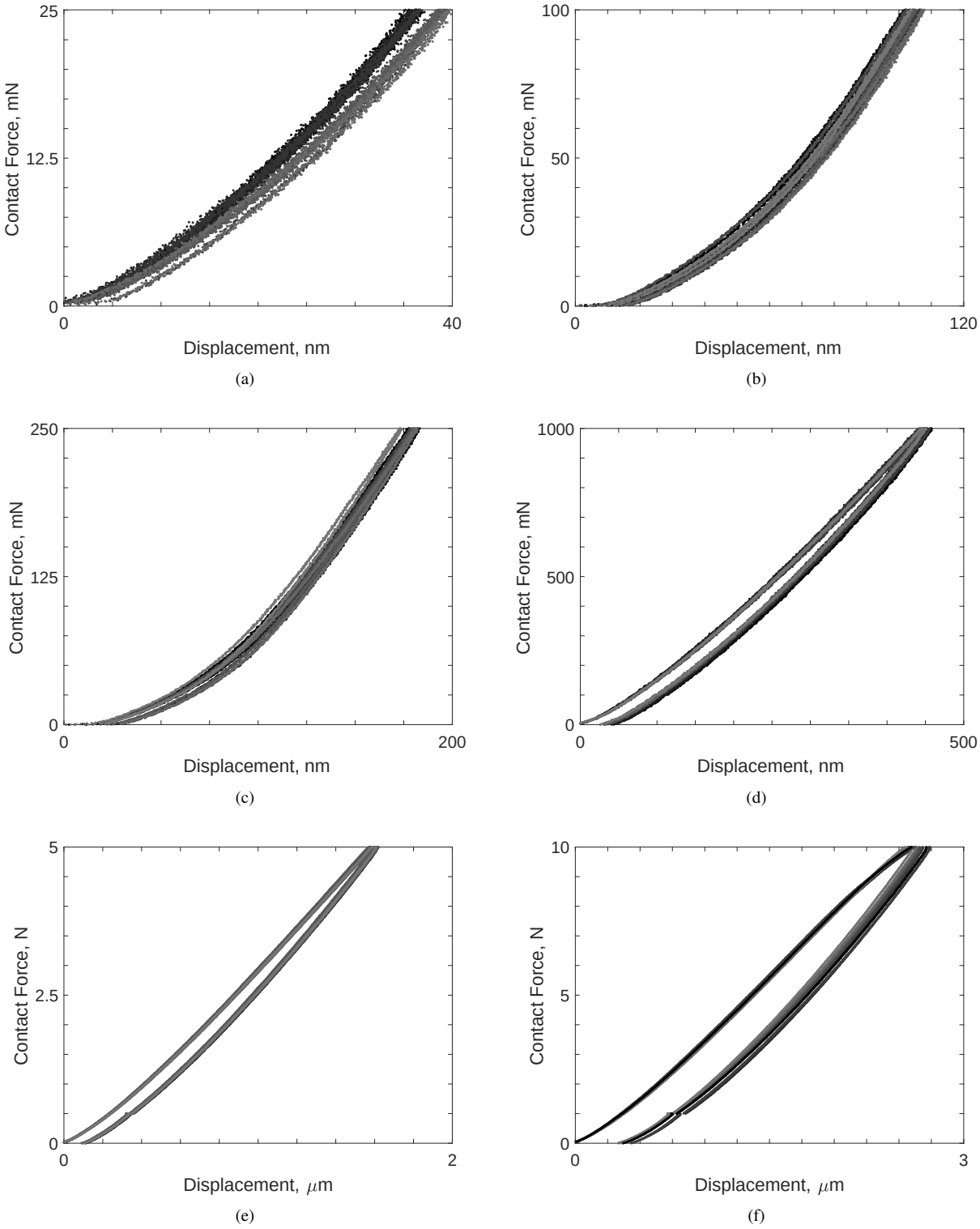

Fig. 26. Compliance measurements of Hiperco indented by the 440c Grade 100 Wear Resistant Stainless Steel sphere for peak loads of (a) 25 mN, (b) 100 mN, (c) 250 mN, (d) 1 N, (e) 5 N, and (f) 10 N. Each load has nine separate measurements.

The compliance measurements for the Hi samples are shown in Fig. 26 for indentation via the 440c sphere, and Fig. 27

for indentation via the Sapphire sphere. In contrast to the previous data sets, the Hi samples exhibit a larger variability at low peak loads for the Sapphire sphere indentations than for the 440c sphere indentations. For the tests at high peak loads, a similar level of repeatability is observed for both indenters, though the 440c sphere measurements exhibit evidence of thermal drift for the highest peak loads (Fig. 26(f)).

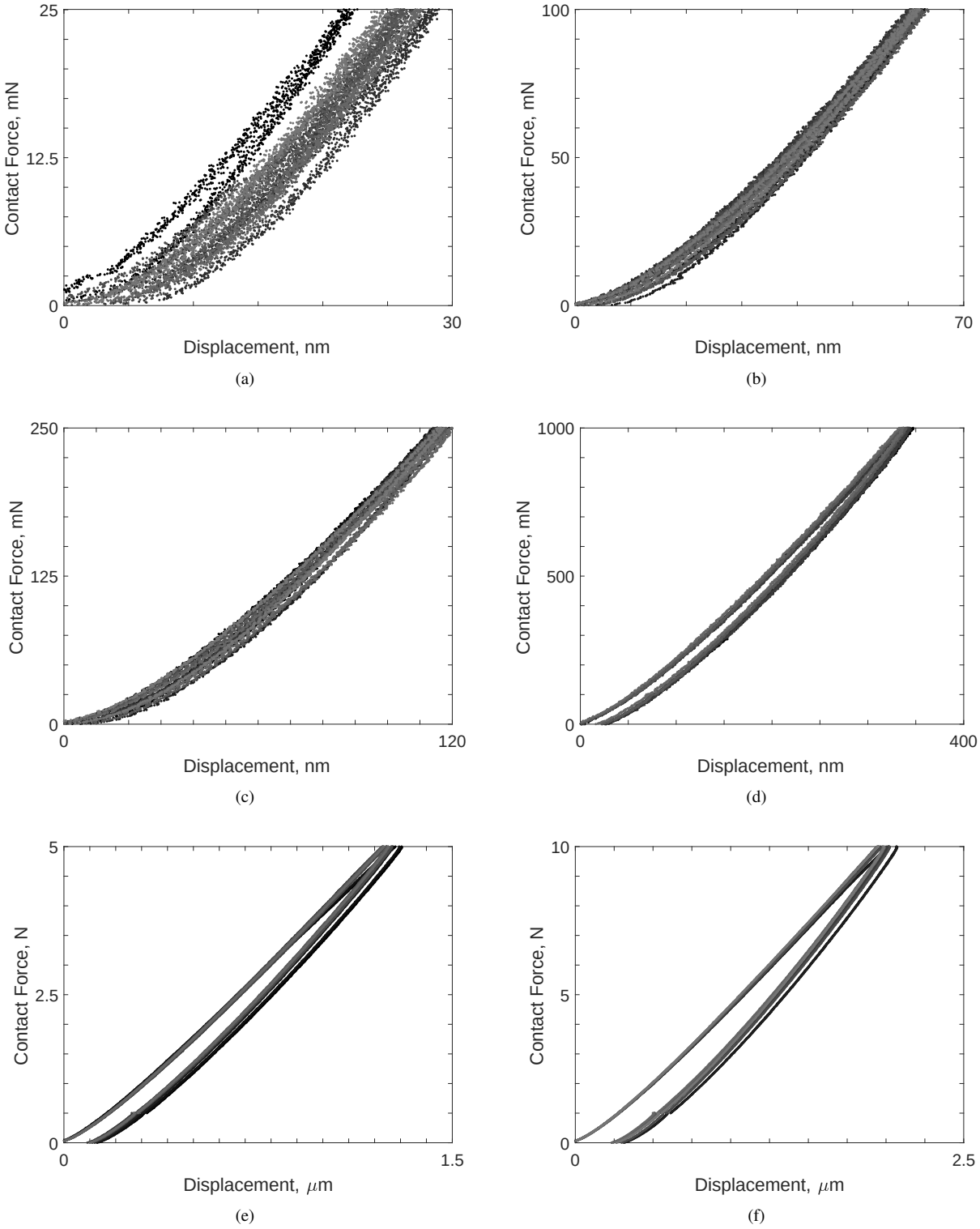

Fig. 27. Compliance measurements of Hiperco indented by the Sapphire sphere for peak loads of (a) 25 mN, (b) 100 mN, (c) 250 mN, (d) 1 N, (e) 5 N, and (f) 10 N. Each load has nine separate measurements.

4.2.5 Nitronic 60A

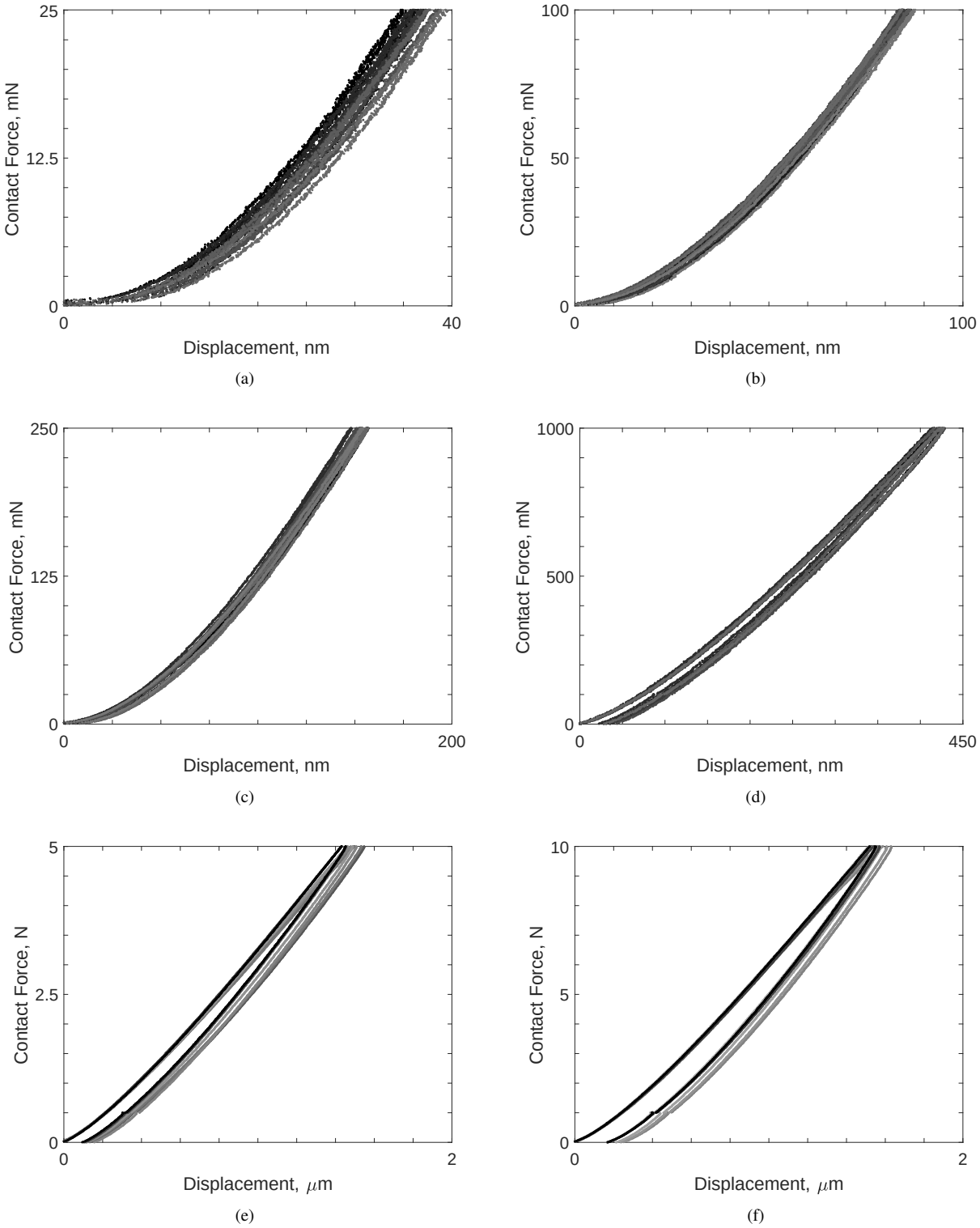

Fig. 28. Compliance measurements of Nitronic 60 indented by the 440c Grade 100 Wear Resistant Stainless Steel sphere for peak loads of (a) 25 mN, (b) 100 mN, (c) 250 mN, (d) 1 N, (e) 5 N, and (f) 10 N. Each load has nine separate measurements.

The compliance measurements for the N60 samples are shown in Fig. 28 for indentation via the 440c sphere, and Fig. 29

for indentation via the Sapphire sphere. The 440c sphere indentation measurements are observed to exhibit more variability for the lowest peak force tested than the Sapphire sphere indentation measurements. All other loads tested exhibited similar repeatability for both indenters.

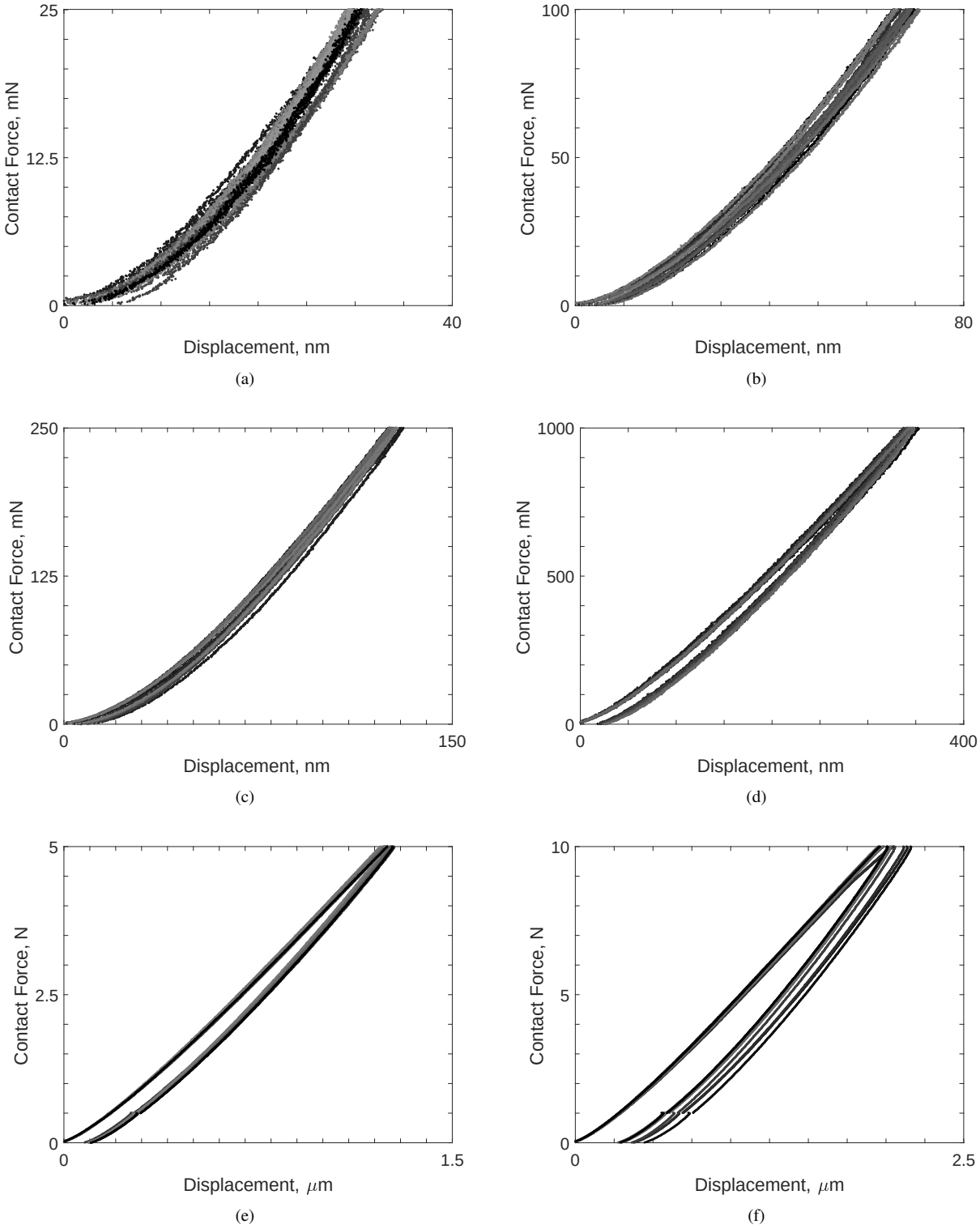

Fig. 29. Compliance measurements of Nitronic 60 indented by the Sapphire sphere for peak loads of (a) 25 mN, (b) 100 mN, (c) 250 mN, (d) 1 N, (e) 5 N, and (f) 10 N. Each load has nine separate measurements.

4.2.6 Phosphor Bronze

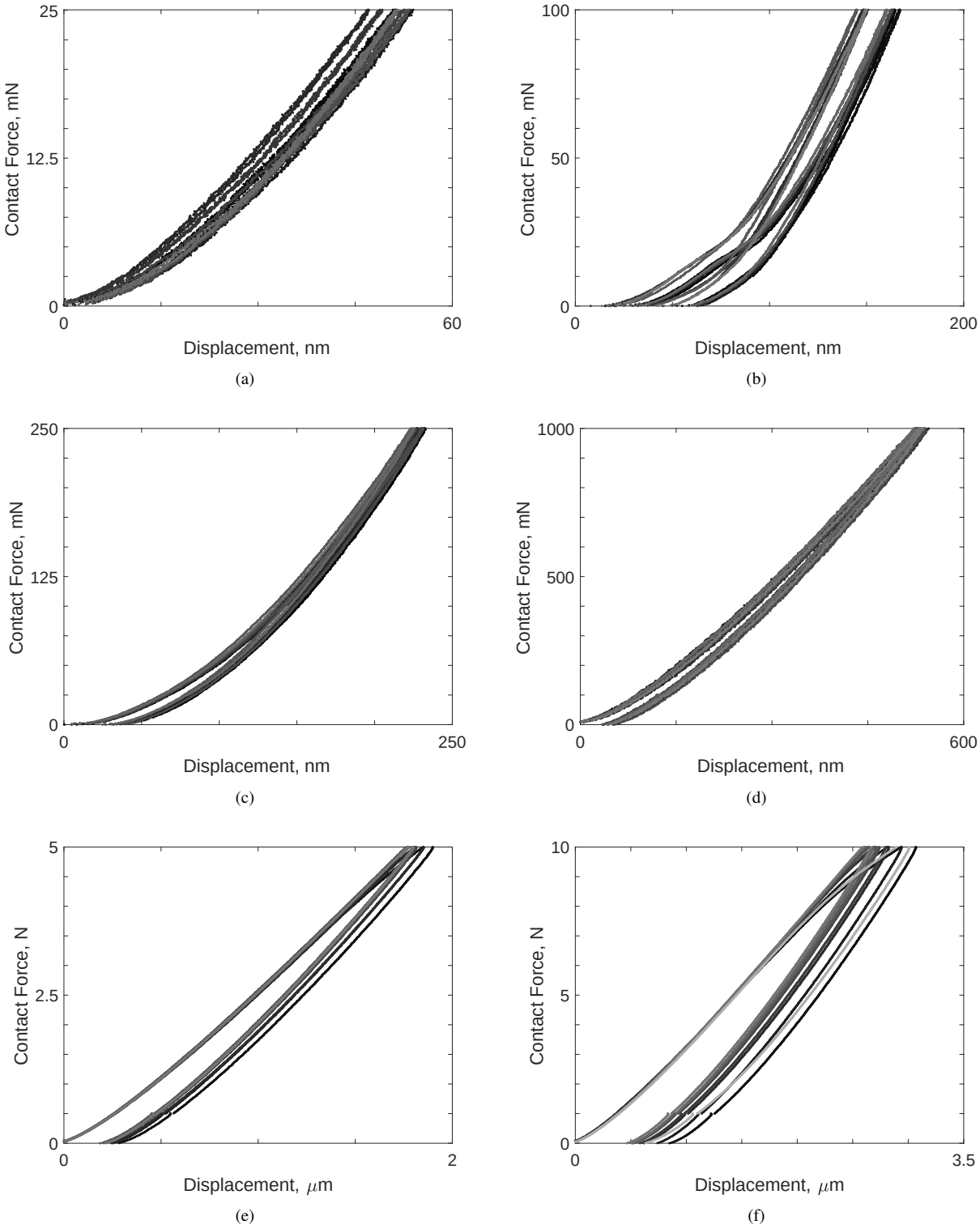

Fig. 30. Compliance measurements of Phosphor Bronze indented by the 440c Grade 100 Wear Resistant Stainless Steel sphere for peak loads of (a) 25 mN, (b) 100 mN, (c) 250 mN, (d) 1 N, (e) 5 N, and (f) 10 N. Each load has nine separate measurements.

The compliance measurements for the PB samples are shown in Fig. 30 for indentation via the 440c sphere, and Fig. 31

for indentation via the Sapphire sphere. While similar repeatability is observed for both indenters, the second load level for the 440c sphere measurements (Fig. 30(b)) exhibits an inflection in the compliance measurement around 75 nm. This inflection is not observed in the Sapphire sphere indentations, and is most likely due to thermal drift.

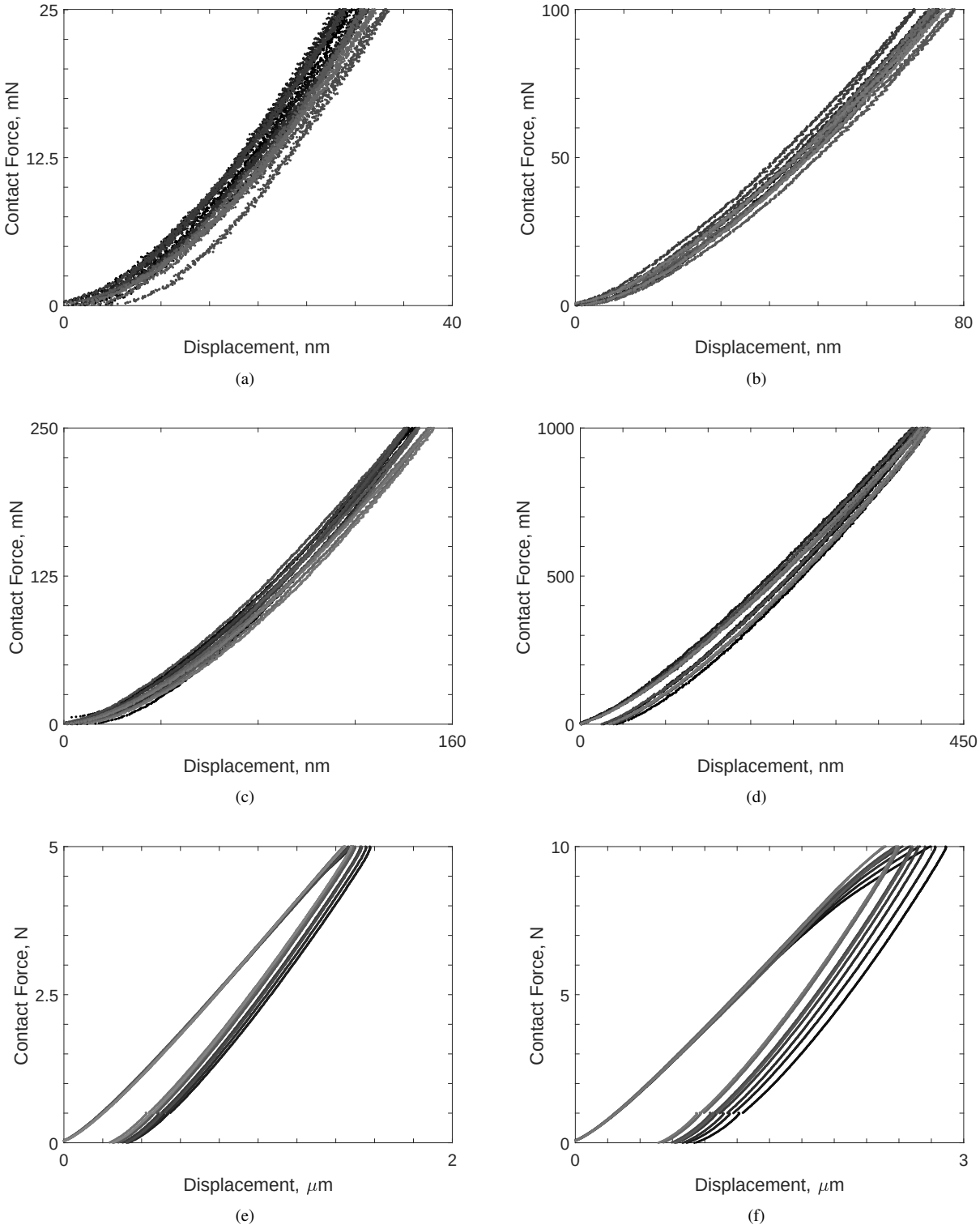

Fig. 31. Compliance measurements of Phosphor Bronze indented by the Sapphire sphere for peak loads of (a) 25 mN, (b) 100 mN, (c) 250 mN, (d) 1 N, (e) 5 N, and (f) 10 N. Each load has nine separate measurements.

A second issue is that the highest peak force tests exhibit thermal drift issues near the peak force for several of the tests by both indenters. This is evidenced by the negative curvature in the loading curves.

4.2.7 Stainless Steel 304

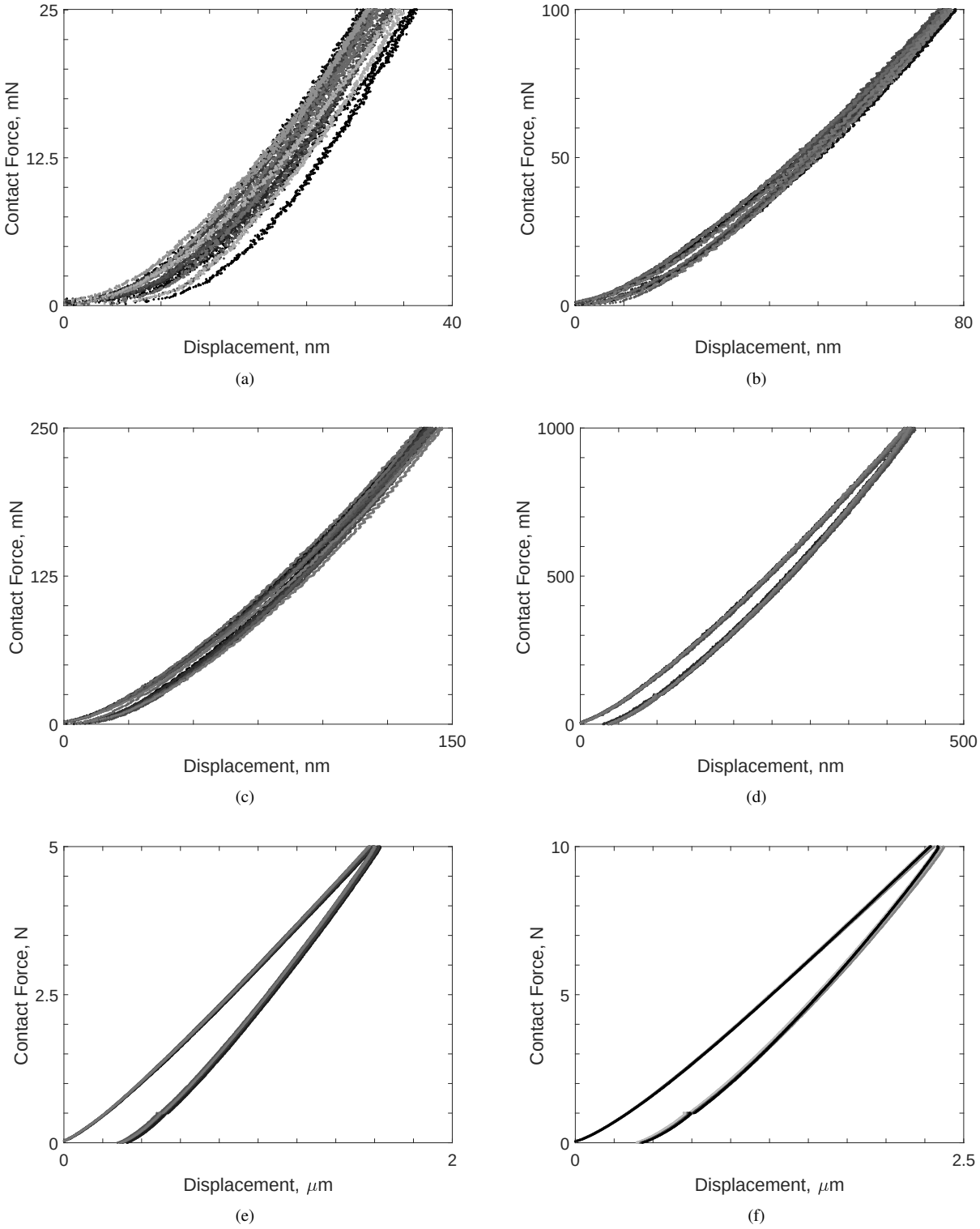

Fig. 32. Compliance measurements of Stainless Steel 304 indented by the 440c Grade 100 Wear Resistant Stainless Steel sphere for peak loads of (a) 25 mN, (b) 100 mN, (c) 250 mN, (d) 1 N, (e) 5 N, and (f) 10 N. Each load has nine separate measurements.

The compliance measurements for the SS304 samples are shown in Fig. 32 for indentation via the 440c sphere, and Fig. 33 for indentation via the Sapphire sphere. Similar repeatability is observed for both indenters.

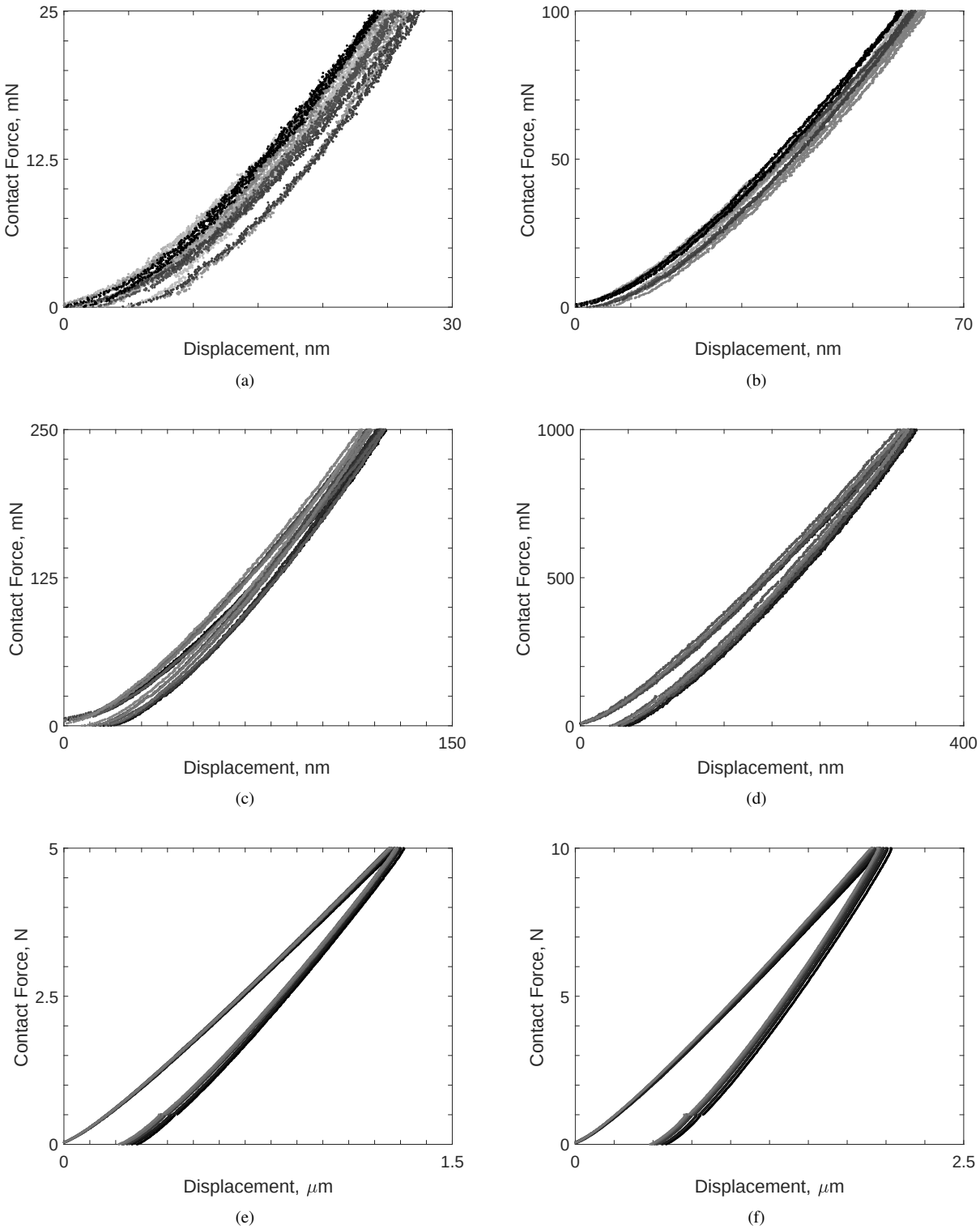

Fig. 33. Compliance measurements of Stainless Steel 304 indented by the Sapphire sphere for peak loads of (a) 25 mN, (b) 100 mN, (c) 250 mN, (d) 1 N, (e) 5 N, and (f) 10 N. Each load has nine separate measurements.

4.2.8 Titanium

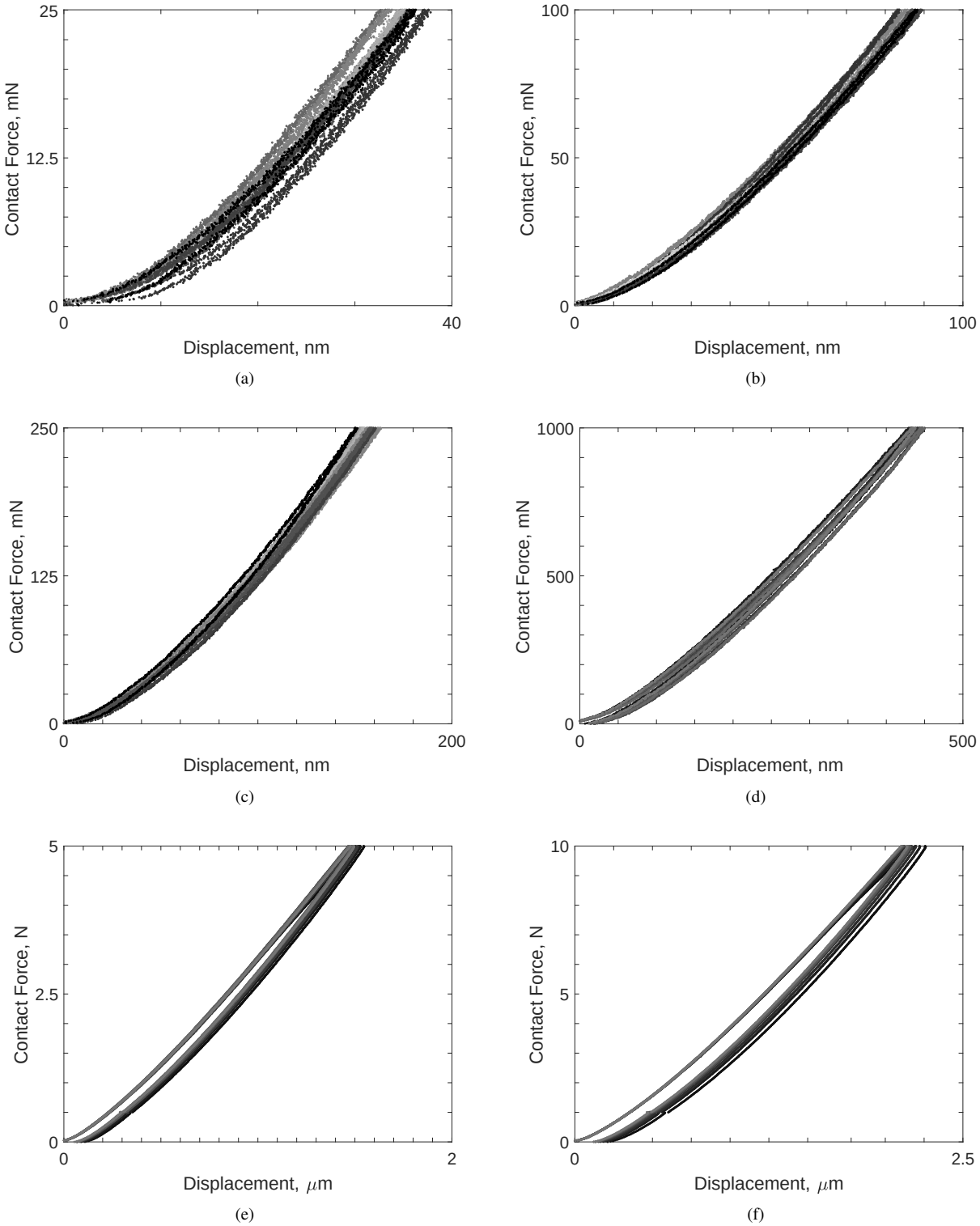

Fig. 34. Compliance measurements of Titanium indented by the 440c Grade 100 Wear Resistant Stainless Steel sphere for peak loads of (a) 25 mN, (b) 100 mN, (c) 250 mN, (d) 1 N, (e) 5 N, and (f) 10 N. Each load has nine separate measurements.

The compliance measurements for the Ti samples are shown in Fig. 34 for indentation via the 440c sphere, and Fig. 35

for indentation via the Sapphire sphere. Like for the SS304 samples, similar repeatability is observed for both indenters.

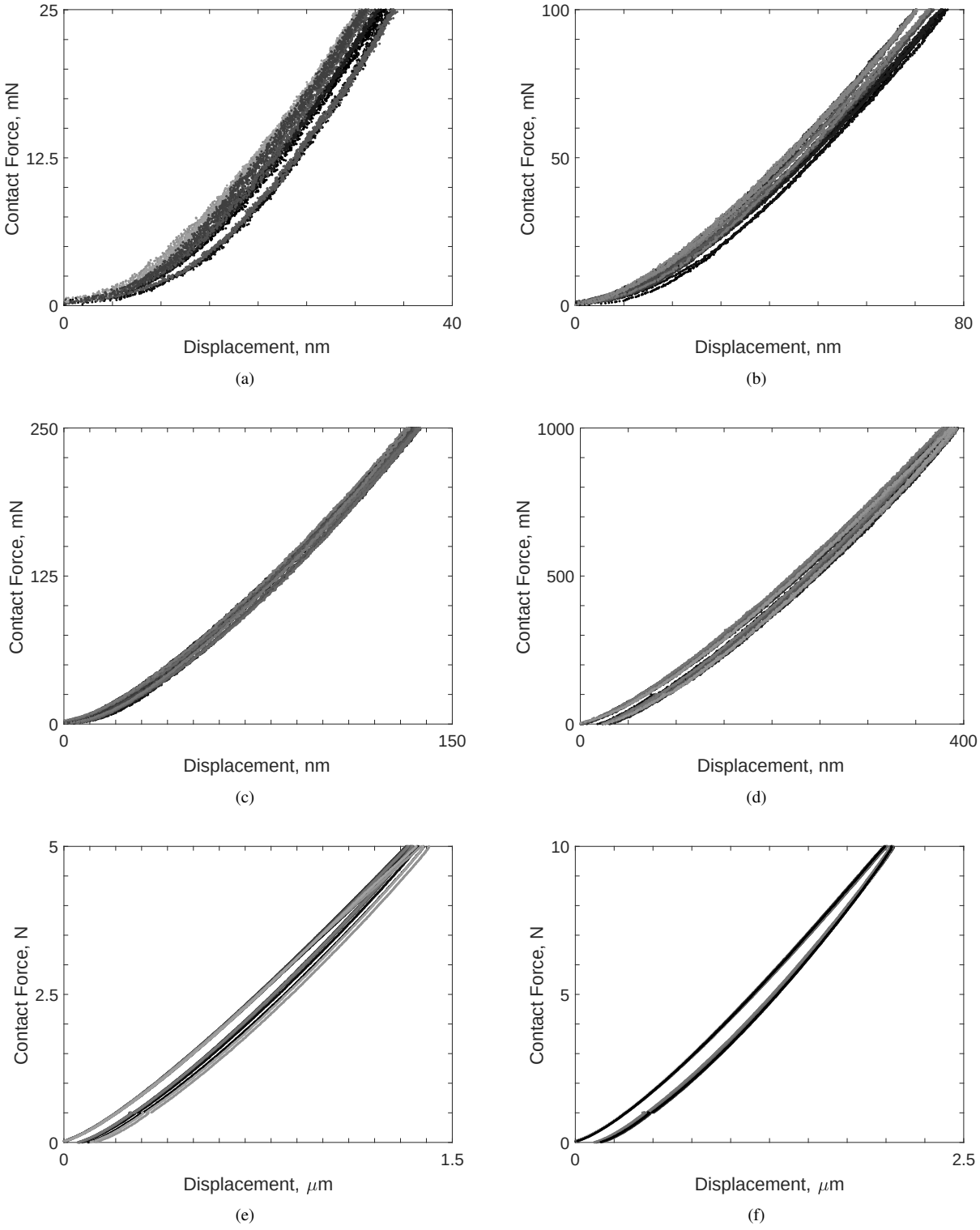

Fig. 35. Compliance measurements of Titanium indented by the Sapphire sphere for peak loads of (a) 25 mN, (b) 100 mN, (c) 250 mN, (d) 1 N, (e) 5 N, and (f) 10 N. Each load has nine separate measurements.

4.3 Discussion of Compliance Measurements

The compliance data were recorded with sub-nm displacement resolution and sub-mN force resolution. These high resolution measurements allow for the study of the material response from the elastic to plastic regime. As is evidenced in Figs. 20 to 35, the transition from elastic behavior to plastic behavior is clearly observable. Data sets with resolution to image the transition from elasticity to plasticity are scarce due to the transition initiating between 2 nm (for AnCu indented by the Sapphire sphere) to 124 nm (for N60 indented by the 440c sphere). The behavior within the elastic regime for metals is well understood, thus the prediction of the inception of plastic behavior is fairly consistent across multiple contact models. Table 5 displays the penetration depth at which the plastic response of the materials initiates, and is based on Hertzian contact theory [33, 34] and the von Mises yeild criterion used in [6, 34, 35]. Note that the values reported in Table 5 are for the inception of yield, which first occurs beneath the surface of the material and is not observable in the compliance data. Once the plastic regime is well-developed, hysteresis is observable in the compliance measurements (i.e. the visible difference between the loading and unloading curves in Figs. 20 to 35).

Material	**440c (nm)**	**Sapphire (nm)**
6061 Aluminum	38.23	29.96
Annealed Copper	2.776	2.016
Copper	7.370	5.203
Hiperco	33.20	19.76
Nitronic 60	123.7	80.06
Phosphor Bronze	23.24	16.76
Stainless Steel 304	96.88	61.23
Titanium	36.43	25.74

Table 5. Predictions of the displacement at which plastic behavior initiates for indentation for both the 440c Grade 100 Wear Resistant Stainless Steel sphere and the Sapphire sphere in the experimental setup of §4 based on the models of [6, 34, 35].

One immediate observation from the comparison of Table 5 to the results of Figs. 20 to 35 is that the predictions for the onset of yield occur for the lowest peak load (i.e. 25 mN) in all materials except N60 and SS304, which have incipient yield between 100 mN and 250 mN. This further highlights the importance of high resolution data at low loads. These predictions are in agreement with the experimental observations, as the hysteresis due to the formation of a plastic zone is not evident until higher peak loads.

5 Conclusions

In this research, eight different materials that are commonly found in aerospace applications were studied. The mechanical properties of each material were characterized, the dissipative properties were measured (in terms of the coefficient of restitution), and the compliance relationships were measured via a micro- and a nano-indentation machine. These two phenomenologically different measurements of contact, coefficient of restitution measurements and compliance measurements, provide both indirect and direct validation metrics. As it is possible (and common) for contact models to agree with one set of metrics but not another, both are needed for the model validation process.

To characterize the dissipative properties of the materials, a pendulum test stand was developed. In this test stand, a 440c Grade 100 Wear Resistant Stainless Steel was used to impact each of the samples. Through the use of digital image correlation, the motion of the sphere is recorded with sub-μm resolution in space and sub-ms resolution in time, allowing for accurate measurements of the coefficient of restituion across an impact event. Additionally, through the use of a circuit closed during contact between the sphere and test specimen, the contact durations for each impact were recorded with microsecond accuracy. The pairing of both contact duration and dissipative properties is paramount for model validation as impact is not an instantaneous event (as the coefficient of restitution model assumes). These two sets of information allow for a more complete understanding of the impact processes.

The compliance relationships for each specimen was measured using two different indenters, a 440c Grade 100 Wear Resistant Stainless Steel sphere and a Sapphire sphere. Additionally, two different indentation machines were used, a micro-indentation machine and a nano-indentation machine, each of which is able to span a different range of peak forces spanning

25 mN to 10 N peak loads in the reported experiments. Predictions from widely used contact theories indicate that for six of the eight materials tested, the inception of yield occurs near 25 mN, which indicates the importance of having high resolution data for low contact forces in order to validate models that span the transition from elastic to plastic behavior.

It is the hope of the authors that this set of data can serve as a complete body of work for the formulation and validation of contact models. Combining the extensive material characterization with two phenomenologically different measures of impact (coefficients of restitution and compliance measurements) provides an opportunity to test and challenge hypotheses for the mechanics of contact. Consequently, all data is freely available from the corresponding author for future investigations.

Acknowledgments

The authors would like to thank the many colleagues that assisted in these experiments over the five years that data was collected: Anton Sumali, Doug VanGoethem, Mike Bejarano, Renee Baca, Somuri Prasad, Jon-Eric Mogonye, Bryan Kuhr, Rand Garfield, Alex Hielo, Carl Stahoviak, and Chris Volk. Additionally, the authors would like to thank Dan Rader, Marcey Hoover, and Mike Chiesa for their support.

References

[1] Cusumano, J. P., and Bai, B.-Y., 1993. "Period-infinity periodic motions, chaos and spatial coherence in a 10 degree of freedom impact oscillator". *Chaos, Solitons and Fractals,* ***3***, pp. 515–536.

[2] Hunt, K. H., and Crossley, F. R. E., 1975. "Coefficient of restitution interpreted as damping in vibroimpact". *ASME Journal of Applied Mechanics,* ***42***, pp. 440–4453.

[3] Whiston, G. S., 1987. "On the statistics of chaotic vibro-impact". *Journal of Sound and Vibration,* ***116***, pp. 598–603.

[4] Butcher, E. A., 1999. "Clearance effects on bilinear normal mode frequencies". *Journal of Sound and Vibration,* ***224***, pp. 305–328.

[5] Brake, M. R., 2012. "An analytical elastic-perfectly plastic contact model". *International Journal of Solids and Structures,* ***49***, pp. 3129–3141.

[6] Brake, M. R. W., 2015. "An analytical elastic plastic contact model with strain hardening and frictional effects for normal and oblique impacts". *International Journal of Solids and Structures,* ***62***, pp. 104–123.

[7] Stronge, W. J., 2000. *Impacts in Mechanical Systems: Analysis and Modelling*, Vol. 551. Springer, ch. Contact Problems for Elasto-Plastic Impact in Multi-Body Systems, pp. 189–234.

[8] Zhang, X., and Vu-Quoc, L., 2002. "Modeling the dependence of the coefficient of restitution on the impact velocity in elasto-plastic collisions". *International Journal of Impact Engineering,* ***27***, pp. 317–341.

[9] Jackson, R. L., Green, I., and Marghitu, D. B., 2010. "Predicting the coefficient of restitution of impacting elastic-perfectly plastic spheres". *Nonlinear Dynamics,* ***60***, pp. 217–229.

[10] Schwager, T., and Pöschel, T., 1998. "Coefficient of normal restitution of visous particles and cooling rate of granular gases". *Physical Review E,* ***57***, pp. 650–654.

[11] Ramírez, R., Pöschel, T., Brilliantov, N. V., and Schwager, T., 1999. "Coefficient of restitution of colliding viscoelastic spheres". *Physical Review E,* ***60***, pp. 4465–4472.

[12] Storakers, B., Biwa, S., and Larsson, P.-L., 1997. "Similarity analysis of inelastic contact". *International Journal of Solids and Structures,* ***34***, pp. 3061–3083.

[13] Ismail, K. A., and Stronge, W. J., 2008. "Impact of viscoplastic bodies: Dissipation and restitution". *ASME Journal of Applied Mechanics,* ***75***, pp. 061011–1–5.

[14] Brake, M. R., 2014. "The role of epistemic uncertainty of contact models in the design and optimization of mechanical systems with aleatoric uncertainty". *Nonlinear Dynamics,* ***77***, pp. 899–922.

[15] Kharaz, A. H., and Gorham, D. A., 2000. "A study of the restitution coefficient in elastic-plastic impact". *Philosophical Magazine A - Physics of Condensed Matter Structure Defects and Mechanical Properties,* ***80***, pp. 549–559.

[16] Gorham, D. A., and Kharaz, A. H., 2000. "The measurement of particle rebound characteristics". *Powder Technology,* ***112***, pp. 193–202.

[17] Minamoto, H., and Kawamura, S., 2009. "Effects of material strain rate sensitivity in low speed impact between two identical spheres". *International Journal of Impact Engineering,* ***36***, pp. 680–686.

[18] Tatara, Y., and Moriwaki, N., 1982. "Study on impact of equivalent two bodies (coefficients of restitution of spheres of brass, lead, glass, porcelain and agate, and the material properties)". *Bulletin of the JSME,* ***25***, pp. 631–637.

[19] Minamoto, H., and Kawamura, S., 2011. "Moderately high speed impact of two identical spheres". *International Journal of Impact Engineering,* ***38***, pp. 123–129.

[20] Alcalá, J., Giannakopoulos, A. E., and Suresh, S., 1998. "Continuous measurements of load-penetration curves with spherical microindenters and the estimation of mechanical properties". *Journal of Materials Research,* ***13***, pp. 1390–1400.

[21] Bolshakov, A., and Pharr, G. M., 1998. "Influences of pileup on the measurement of mechanical properties by load and depth sensing indentation techniques". *Journal of Materials Research,* ***13***, pp. 1049–1058.
[22] Swadener, J. G., Taljat, B., and Pharr, G. M., 2001. "Measurement of residual stress by load and depth sensing indentation with spherical indenters". *Journal of Materials Research,* ***16***, pp. 2091–2102.
[23] Jamari, J., and Schipper, D. J., 2006. "Experimental investigation of fully plastic contact of a sphere against a hard flat". *ASME Journal of Tribology,* ***128***, pp. 230–235.
[24] Ovcharenko, A., Halperin, G., Verberne, G., and Etsion, I., 2007. "In situ investigation of the contact area in elastic-plastic spherical contact during loading-unloading". *Tribology Letters,* ***25***, pp. 153–160.
[25] Alcalá, J., and de los Ojos, D. E., 2010. "Reassessing spherical indentation: Contact regimes and mechanical property extraction". *International Journal of Solids and Structures,* ***47***, pp. 2714–2732.
[26] Bartier, O., Hernot, X., and Mauvoisin, G., 2010. "Theoretical and experimental analysis of contact radius for spherical indentation". *Mechanics of Materials,* ***42***, pp. 640–656.
[27] Jackson, R. L., and Kogut, L., 2006. "A comparison of flattening and indentation approaches for contact mechanics modeling of single asperity contacts". *ASME Journal of Tribology,* ***128***, pp. 209–212.
[28] Tabor, D., 1948. "A simple theory of static and dynamic hardness". *Proceedings of the Royal Society of London, Series A,* ***192***, pp. 247–274.
[29] Sutton, M. A., Orteu, J.-J., and Schreier, H. W., 2009. *Image Correlation for Shape, Motion and Deformation Measurements: Basic Concepts, Theory and Applications*. Springer, New York.
[30] Reu, P. L., and Miller, T. J., 2008. "The application of high-speed digital image correlation". *The Journal of Strain Analysis for Engineering,* ***43***, pp. 673–688.
[31] Reu, P. L., Sweatt, W., Miller, T., and Fleming, D., 2015. "Camera system resolution and its influence on digital image correlation". *Experimental Mechanics,* ***55***, pp. 9–25.
[32] Mogonye, J.-E., and Prasad, S. V., 2014. "Novel nano-impact techniques for determining the onset of fracture in brittle films". In International Conference on Metallurgical Coatings and Thin Films.
[33] Hertz, H., 1882. "Über die berührung fester elastischer körper (On the contact of elastic solids)". *Journal fur die Reine und Andgewandte Mathematik,* ***92***, pp. 156–171.
[34] Johnson, K. L., 1985. *Contact Mechanics*. Cambridge University Press, Cambridge.
[35] Vu-Quoc, L., Zhang, X., and Lesburg, L., 2000. "A normal force-displacement model for contacting spheres accounting for plastic deformation: Force-driven formulation". *ASME Journal of Applied Mechanics,* ***67***, pp. 363–371.